Supplementary Information (SI) for Energy & Environmental Science.

Supporting Information

Neighboring Iron Single Atomic Sites Boost PtCo Intermetallic for High-Durability ORR Electrocatalysis

Kai Chen,[a,b] Junheng Huang,[a] Junxiang Chen,[a] Jiyuan Gao,[a,b] Zhiwen Lu,[a,b] Xi Liu,[a,] Senchen Lan,[c] Guohua Jia,[d,*] Suqin Ci,[c,*] and Zhenhai Wen,[a,*]

[a] State Key Laboratory of Structural Chemistry, and Fujian Provincial Key Laboratory of Materials and Techniques toward Hydrogen Energy, Fujian Institute of Research on the Structure of Matter, Chinese Academy of Sciences, Fuzhou, Fujian, 350002, China.

[b] University of Chinese Academy of Sciences, Beijing, 100049, China.

[c] Fujian Provincial Key Laboratory of Soil Environmental Health and Regulation, College of Resources and Environment, Fujian Agriculture and Forestry University, Fuzhou 350002, China

[d] School of Molecular and Life Sciences, Curtin University, Bentley, WA 6102, Australia

[*] Corresponding authors.

E-mail: Guohua.Jia@curtin.edu.au; sqci@fafu.edu.cn; wen@fjirsm.ac.cn

1. Experimental Details

1.1 Chemicals and materials

Zinc nitrate hexahydrate ($Zn(NO_3)_2{\cdot}6H_2O$, 98%), 2-methylimidazole ($C_4H_6N_2$, 98%), iron (III) acetylacetonate ($Fe(C_5H_7O_2)_3$, 98%), Chloroplatinic acid hexahydrate ($H_2PtCl_6{\cdot}6H_2O$, 99%), Cobalt chloride hexahydrate ($CoCl_2{\cdot}6H_2O$, 99%), concentrated sulfuric acid (H_2SO_4, 98%) and Potassium hydroxide (KOH, 85%) were purchased from Aladdin Reagent (Shanghai) Co., Ltd. All the reagents were used directly without further purification.

1.2. Synthesis of the materials

Synthesis of FeNC

2-methylimidazole (4.000 g) was dissolved in 90 mL methanol in flask A. $Zn(NO_3)_2{\cdot}6H_2O$ (3.630 g) and iron (III) acetylacetonate (0.300 g) were dissolved in 60 mL methanol in flask B. Flask B was subsequently added into flask A with stirring for 20 h at room temperature. The product was separated by centrifugation and washed with methanol for five times and finally dried at 60°C under vacuum for 10 h. Lastly, the obtained faint yellow powder (Fe-ZIF-8) was pyrolyzed at 950°C for 2 hours in flowing argon atmosphere with a heating rate of 5 °C min^{-1}.

Synthesis of NC

Like the synthesis of FeNC, but without the addition of iron acetylacetonate.

Synthesis of O-PtCo-FeNC and O-PtCo-NC

100 mg FeNC powder was ultrasonically dispersed in 20 mL deionized water for 1h, then 4.0 mL 10 mg mL^{-1} $H_2PtCl_6{\cdot}6H_2O$ and 3.62 mL of 5 mg mL^{-1} $CoCl_2{\cdot}6H_2O$ were added, and after ultrasonic treatment for 1h, freeze drying was carried out. Then, it was kept at 800°C for 2 hours in 10% H_2/Ar atmosphere with a heating rate of 5 °C min^{-1}. The synthesis of O-PtCo-NC is similar, except that NC was used instead of FeNC.

Synthesis of D-PtCo-FeNC and D-PtCo-NC

The difference from the synthesis of ordered alloy was that the pyrolysis temperature was changed to 600°C.

1.3. Physical Characterizations

X-ray diffraction (XRD) patterns were acquired on X-ray diffractometer (Miniflex6000, Rigaku) at 40 kV and 15 mA using Cu- Kα radiation (λ= 1.54178 Å). The Raman spectra of the catalysts were tested on Labram HR800 Evolution in the range of 500-4000 cm^{-1}. X-ray photoelectron spectroscopy (XPS) tests were employed on Thermo Scientific K-Alpha. The scanning electron microscope patterns (SEM) and transmission electron microscope patterns (TEM) were recorded on Zeiss Sigma 300 and FEI Titan G2 60-300.

Data reduction, data analysis, and EXAFS fitting were performed and analyzed with the Athena and Artemis programs of the Demeter data analysis packages[1] that utilizes the FEFF6 program[2] to fit the EXAFS data. The energy calibration of the sample was conducted through standard and Fe and Co foil, which as a reference was simultaneously measured. A linear function was subtracted from the pre-edge region, then the edge jump was normalized using Athena software. The $\chi(k)$ data were isolated by subtracting a smooth, third-order polynomial approximating the absorption background of an isolated atom. The k^3-weighted $\chi(k)$ data were Fourier transformed after applying a Hanning window function ($\Delta k = 1.0$). For EXAFS modeling, The global amplitude EXAFS (*CN, R,* σ^2 and ΔE_0) were obtained by nonlinear fitting, with least-squares refinement, of the EXAFS equation to the Fourier-transformed data in *R*-space, using Artemis software, EXAFS of the Fe and Co foil are fitted and the obtained amplitude reduction factor S_0^2 value (0.76) was set in the EXAFS analysis to determine the coordination numbers (*CNs*) for each scattering path in sample. For Wavelet Transform analysis, the $\chi(k)$ exported from Athena was imported into the Hama Fortran code. The parameters were listed as follow: R range, 1 – 4 Å, k range, 1 - 12.0 Å^{-1}.

2. Electrochemical characterization

2.1 Electrochemical measurements

Oxygen reduction reaction properties were obtained by a three-electrode system on a CHI760 electrochemical station (CH instrument Co.) at 25°C. A carbon electrode, Ag/AgCl electrode and rotating disk electrode (RDE)/rotating ring-disk electrode (RRDE) were served as counter electrode, reference electrode and working electrode, respectively. 5.0 mg catalysts, including 20 wt% Pt/C, were ultrasonically dispersed in solution (1 mL) containing Nafion (50 μL), ethanol (400 μL) and water (550 μL) for 1 hour to form homogeneous electrocatalysts ink. The O_2-saturated 0.5 M H_2SO_4 served as the medium for ORR without ohmic compensation. For CV measurement, scan rate was 50 mV s^{-1}, for the RDE/RRDE tests were 10 mV s^{-1}. CV tests were conducted at various scan rates in the non-Faradic region to calculate the double-layer capacitance of different materials throughout the cycle. Simultaneously, electrochemical impedance was measured during the cycle over a frequency range of 0.1 to 100,000 Hz, using the open circuit voltage as the initial value.

The experiments were performed using an electrochemical Raman device and a HORIBA confocal Raman spectrometer. An oxygen-saturated 0.5 M H_2SO_4 solution was used as the electrolyte and the catalyst was drop-coated on carbon paper to form a gas diffusion electrode. A 532 nm wavelength laser was used during the experiments with an intensity level of 5%. Raman spectra were collected in the range of 800 - 2000 cm^{-1}, with data acquisition lasting 12 seconds per scan and repeated 12 times.

2.2 Data analysis

All the potentials were shift to a reversible hydrogen electrode (RHE): $E_{RHE} = E_{Ag/AgCl} + 0.059\ V \times pH$.

The electron transfer number (n) were acquired by the Koutecky-Levich (K-L) eq. (1):

$$\frac{1}{J} = \frac{1}{J_L} + \frac{1}{J_K} = \frac{1}{Bw^{1/2}} + \frac{1}{J_K} \qquad (1)$$

J is the measured current density; J_K and J_L are the kinetic and limiting current densities, respectively; w is the linear rotation speed (rpm s^{-1}) of the disk.

The H_2O_2 yield and the electron transfer number (n) on RRDE at 1600 rpm were obtained by the eq. (2) and eq. (3):

$$H_2O_2\% = 200 \times \frac{I_r/N}{I_d + I_r/N} \qquad (2)$$

$$n = 4 \times \frac{I_d}{I_d + I_r/N} \qquad (3)$$

Where I_d, I_r and N (0.40) are the disk current, ring current and ring collection efficiency, respectively. To determine the collection coefficient of the ring-disk electrode, linear sweep voltammetry experiments were conducted at various rotation speeds in an electrolyte containing 5 mM $K_3[Fe(CN)_6]$ and 100 mM KCl, using a scan rate of 10 mV s^{-1}. Theory suggests that N should be independent of rotation speed, and our results support this: using the relationship $N = I_r/I_d$, we consistently obtained a value of 0.40 across all speeds (Fig S17d).

The mass activity (MA) and specific activity (SA) are calculated according to eq. (4) and eq. (5).

$$MA = \frac{j_k}{m_{pt}} \qquad (4)$$

$$\mathrm{SA} = \frac{j_k}{ECSA} \tag{5}$$

The electrochemical surface area (ECSA) of the catalyst can be estimated using the hydrogen underpotential deposition (Hupd) method. Additionally, the Hupd method, with a calibration factor of 210 μC cm^{-2}, was used to assess the ECSA. The Hupd measurements were performed in 0.5 M H_2SO_4 saturated with N_2 at a scan rate of 50 mV s^{-1}. The potential range for the Hupd adsorption/desorption peaks, from approximately 0.06 V to 0.410 V after subtracting the capacitive current, was used to obtain the charge (Q_H). The baseline for integrating the Q_H associated with the Hupd adsorption/desorption peaks was taken as the current value at approximately 0.40 V. The ECSA estimated using the Hupd method was calculated according to Eq. (6).

$$\mathrm{ECSA} = \frac{Q_H}{210 * m_{pt}} \tag{6}$$

Here, m_{Pt} refers to the Pt loading of the catalyst used in the working electrode. The ECSA is estimated by averaging the charge associated with H adsorption and desorption peaks for comparison. Finally, the stability of catalysts was evaluated by performing accelerated durability testing (ADT) in an O_2 atmosphere, using a potential range of 0.6 - 1.0 V (*vs.* RHE) with a scan rate of 100 mV s^{-1}, and assessing performance over 10k, 30k and 50k cycles.

3. Operando characterization

The in-situ infrared testing involves utilizing attenuated total reflection-surface enhanced infrared absorption spectroscopy (ATR-SEIRAS) measurements conducted with a Bruker 70 V Fourier transform infrared (FTIR) spectrometer. During the measurement process, the spectral resolution is set to 8 cm^{-1}, and each spectrum was obtained by accumulating 120 interference patterns after a constant voltage test of 300 s. The preparation of the working electrode comprises two crucial steps: firstly, an ultra-thin gold film is deposited onto the Si crystal using chemical deposition technology. Secondly, catalyst ink is dispensed onto the Au film with a loading density of 0.1 mg cm^{-2}. Following this, the Si crystal, now laden with the catalyst, is securely positioned at the testing site of the spectroelectrochemical three-electrode cell. In this cell configuration, the Ag/AgCl electrode serves as the reference electrode, while a Pt wire functions as the counter electrode. The electrolyte employed in this setup is a 0.5 M H_2SO_4 solution.

The in-situ Raman spectra were recorded using a Horiba LabRam Aramis HR evolution confocal Raman spectrometer, employing a 532 nm laser. An in-situ Raman spectroelectrochemical device featuring a gas-solid-liquid interface was utilized to analyze the signals of surface-related compounds present in the target sample at various potentials. The spectral resolution was set to 4 cm^{-1}, and at each voltage, the acquisition process involved accumulating data for 300 seconds, with each acquisition lasting 12 seconds and repeated 12 times.

4. Configuration and measurement of Zn-air batteries

10.0 mg O-PtCo-FeNC catalysts, 20 wt% Pt/C, were ultrasonically dispersed in solution (1 mL) containing Nafion (50 μL), ethanol (400 μL) and water (550 μL) for 1h to form homogeneous electrocatalysts ink. For hybrid acid/alkali Zn-air batteries: A 3 cm * 3 cm zinc plate was utilized as anode; 2.0 M H_2SO_4 and 4.0 M KOH solutions were employed as the cathode and anolyte, respectively; Nafion 117 (DuPont) that had been immersed in 1 M KCl solution for 12 hours was employed as a cation exchange membrane. This membrane served to separate the anode and cathode electrolytes while facilitating ion transport. The distance between the cathode and anode was maintained at 4 mm. Subsequently, 150 μL of the catalyst ink was drop-cast onto a 1 cm^2 piece of carbon paper and allowed to dry naturally to form the air cathode. Peristaltic pumps were used to circulate 100 mL of both the catholyte and anolyte. For alkali Zn-air batteries: A 6 M KOH solution was used as the electrolyte, while all other parameters were kept unchanged. The LAND-CT-3002K testing devices were used to analyze the battery discharge performance. The discharge curves were recorded in ambient on a CHI 760E electrochemical workstation with a CHI 680C high current amplifier.

ORR at the cathode (acid, 2.0 M H_2SO_4, $E^{\theta}_{O_2/H_2O} = 1.23\ V\ vs.\ RHE$):

$$O_2 + 4H^+ + 4e^- \rightarrow 2H_2O \tag{R1}$$

$$E_c = E^{\theta}_{O_2/H_2O} + 2.303\frac{RT}{4F}\log\left[\left(\alpha_{H^+}\right)^4\right] = 1.23\ V + 0.0592 * \log\left(\alpha_{H^+}\right) = 1.266\ V \qquad \text{(Eq. 1)}$$

ORR at the cathode (alkaline, 6.0 M KOH, $E^{\theta}_{O_2/OH^-} = 0.401\ V\ vs.\ RHE$):

$$O_2 + 2H_2O + 4e^- \rightarrow 4OH^- \tag{R2}$$

$$E_c = E^{\theta}_{O_2/OH^-} - 2.303\frac{RT}{4F}\log\left[\left(\alpha_{OH^-}\right)^4\right] = 0.401\ V - 0.0592 * \log\left(\alpha_{OH^-}\right) = 0.355\ V \qquad \text{(Eq. 2)}$$

Oxidation of Zn at the anode (alkaline, $E^{\theta}_{Zn^{2+}/Zn} =- 1.249\ vs.\ RHE$):

$$Zn - 2e^- + 2OH^- \rightarrow ZnO + H_2O \tag{R3}$$

$$E_a = E^{\theta}_{Zn^{2+}/Zn} - 2.303\frac{RT}{2F}\log\left[\left(\alpha_{OH^-}\right)^2\right] =- 1.249 - 0.0592 * \log\left(\alpha_{OH^-}\right) \tag{Eq. 3}$$

In 4 M KOH $E_a =- 1.284$ V, in 6 M KOH $E_a =- 1.295$ V.

Theoretical voltage of hybrid Zn-air batteries

Overall reaction:

$$2Zn + O_2 + 4H^+ + 4OH^- \rightarrow 2ZnO + 4H_2O \tag{R4}$$

$$V_{cell} = E_c - E_a = 1.266 - (- 1.284) = 2.550\ V \tag{Eq. 4}$$

The theoretical energy density of hybrid acid/alkali Zn-air batteries.

$$E_{theo} = C_{theo} * V_{cell} = 0.82\ Ah\ g^{-1} * 2.55\ V = 2091\ Wh\ kg^{-1} \tag{Eq. 5}$$

Theoretical voltage of an alkaline Zn-air battery in 6 M KOH

Overall reaction:

$$2Zn + O_2 + \rightarrow 2ZnO \tag{R5}$$

$$V_{cell} = E_c - E_a = 0.355 - (- 1.295) = 1.65\ V \tag{Eq. 6}$$

The theoretical energy density of alkaline Zn-air batteries:

$$E_{theo} = C_{theo} * V_{cell} = 0.82\ Ah\ g^{-1} * 1.65\ V = 1353\ Wh\ kg^{-1} \tag{Eq. 7}$$

The specific capacitor of Zn-air battery was calculated from the following equation in the discharge process at different current density:

$$C_{sp} = \frac{i \times t}{\triangle m} \tag{Eq. 8}$$

Where *i* and *t* are the discharge current and time, respectively, and $\triangle m$ is the weight of Zn used.

5. Theoretical calculations

5.1. Simulation Fundamentals and Methodology

Considering the complexity of the system in this study, which includes a PtCo-graphite/N-doped/single-atom interface, it is necessary to (1) account for the computational load by optimizing the material to the largest possible size and (2) consider the diversity of active sites within this structure. Given that in catalysis, the activity of 1% of the sites often exceeds the combined activity of the remaining 99%, it is crucial to perform calculations for all active sites on the catalyst. These factors render traditional DFT methods based on unit cells ineffective. Consequently, modern machine learning potentials (MLPs) have become important candidates. In this work, we use MLPs (introduced in section 4.4)[3] to optimize the O-PtCo-FeNC and O-PtCo-NC structure and interface model, and to construct the free energy diagram (FED) for all active sites.

5.2. Model Construction

An annealing simulation method was carried out to construct the model. The configurations illustrated in Figure S32 were served as the basis for training our force field (FF). These structures were considered to possess characteristic features of FeN_3-PtCo and NC-PtCo structures. Commencing from these initial structures, we embark on a series of ab initio molecular dynamics (AIMD) simulations spanning a duration of 0.7 ps, during which temperatures are systematically varied from 1000 to 300 K. The integration of these simulations is facilitated by a time step of 1 fs. The resultant AIMD data, inclusive of atomic forces, energies, and local atomic environments, is harnessed in the construction of our machine learning potential, which is rooted in DFT principles. After that, a DPGEN like loop was execute to finetune the force field.[4]

To obtain more accurate structures, after acquiring the force field, an annealing simulation approach was employed for these four samples. The annealing temperature was set from 1500 to 300 K, with temperature control using the Nose-Hoover Thermostat, adjusting the temperature every 100 time steps. The simulation time step was 1 fs, with a total simulation duration of 200 ps. During the simulation, considering the system as an intermetallic compound, we enforced a temperature of 10 K within 2 nm of the PtCo and Pt particles internally to maintain the coordination and crystal structure of the intermetallic compound. All the annealing simulations are executed utilizing the extensive capabilities of the large-scale atomic/molecular massively parallel simulator (LAMMPS).[5]

5.3. Generation of Free energy diagram

The ORR process generally refers to the following classic four-step process:

$$O_2 \rightarrow O_2^*$$

$$O_2^* + H^+ + e^- \rightarrow OOH^*$$

$$OOH^* + H^+ + e^- \rightarrow O^* + H_2O$$

$$O^* + H^+ + e^- \rightarrow OH^*$$

$$OH^* + H^+ + e^- \rightarrow H_2O$$

Here, * represents the adsorption site.

we adopted the computational hydrogen electrode (CHE) method to deal with the charged species, including H^+ and e^-.[6] The chemical potential for associated adsorbates were calculated via the following eq. (7):

$$u_A = E_A + ZPE - TS \tag{7}$$

E_A is the total energy of a certain molecule A or adsorbate *A. For molecule, EA can be obtained directly through a gas phase calculation; for a certain adsorbate, E*A is calculated by the difference between the DFT based substrate with (E_{*A}^{DFT}) and without adsorbate A (E_*^{DFT}):

$$E_{*A} = E_{*A}^{DFT} - E_*^{DFT} \tag{8}$$

ZPE and TS are the correction from zero point energy and, entropy, whose values are taken from ref. 6 When calculating adsorbates, a recently developed workflow (https://github.com/cjxxjc729/iterative_surface_oxidation) was used to consider all sites.[7] This workflow automatically analyzes potential surface sites, cuts the nearby structures to construct models, and then automatically adds relevant intermediates along the normal vector of the adsorption site to calculate the corresponding adsorption energies and FED.

5.4. Details of the MLP

The MLP used in this text is a LAM trained through this scheme, named OC_20M.pb (https://github.com/deepmodeling/AIS-Square/tree/main/models/DPA_1_OC2M).[8, 9] It was trained using a subset of the materials database OC20,[10] specifically a subset called OC2M, which contains 2 million data points. The total number of training steps was 20 million (20M). During the training process, the distance cutoff and smoothing lengths were set to 9 Å and 2 Å, respectively. The fitting network's neural network had three layers, each with 240 neurons. The initial and final learning rates were 0.001 and $5e^{-8}$, respectively, with the learning rate decreasing exponentially during the training. The initial and final weights for energy and force were set to 0.02 and 1000, and 2 and 1, respectively. The training involved 3 million steps. For related force field files, one can refer to ref.6, with the only difference being the use of 3 million training steps instead of 1 billion. Additionally, the values of type-embedding exhibited properties close to those of the periodic table, indicating the accuracy of its learning.

5.5. DFT parameters

Spin-polarized DFT calculations were meticulously conducted within periodic super-cells, employing the generalized gradient approximation (GGA) alongside the Perdew-

Burke-Ernzerhof (PBE) functional for exchange-correlation. The expansion of Kohn-Sham orbitals transpired within a plane-wave basis set, characterized by a kinetic energy cutoff of 30 Ry and a charge-density cutoff of 300 Ry. Notably, the point of marginal adsorption energy change resides beyond these values, exhibiting variations within a scant 0.02 eV range. To account for Fermi-surface effects, we judiciously employed the smearing technique introduced by Methfessel and Paxton, leveraging a smearing parameter of 0.02 Ry. Convergence criteria were judiciously established, entailing Cartesian force components acting on each atom to reach a precision of 10^{-3} Ry/Bohr, and a total energy convergence threshold of 10^{-5} Ry. In alignment with the non-periodic nature of molecules, a gamma k-point mesh was uniformly employed to sample the Brillouin zones. To further enhance accuracy, the dispersion correction was consistently incorporated across all calculations, employing the semiempirical zero damping D3 method advanced by Grimme.[11] All the calculations were conducted by the PWSCF codes contained in the Quantum ESPRESSO distribution.[12]

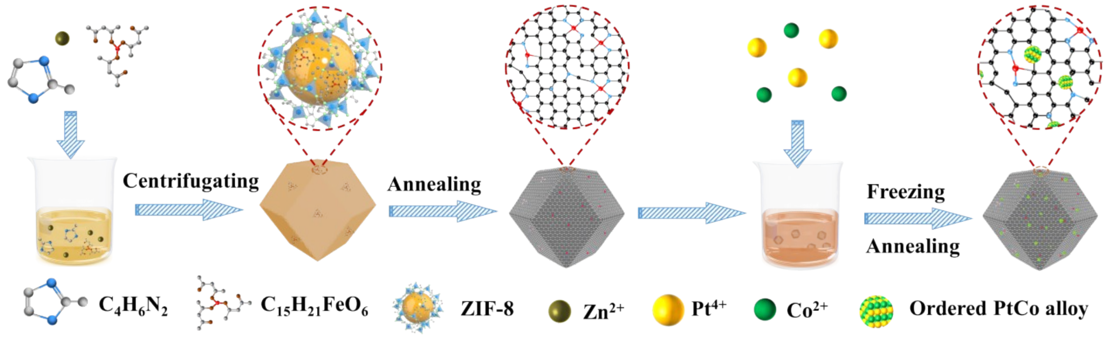

Figure S1. Schematic illustration for the preparation of O-PtCo-FeNC catalyst.

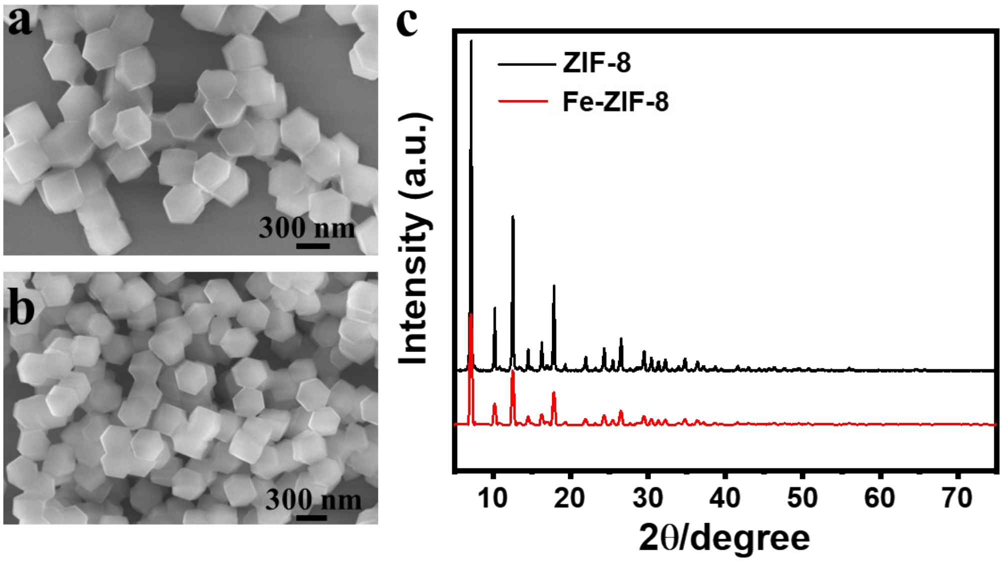

Figure S2. (a) SEM image of ZIF-8, (b) SEM image of Fe-ZIF-8, (c) XRD patterns of ZIF-8 and Fe-ZIF-8.

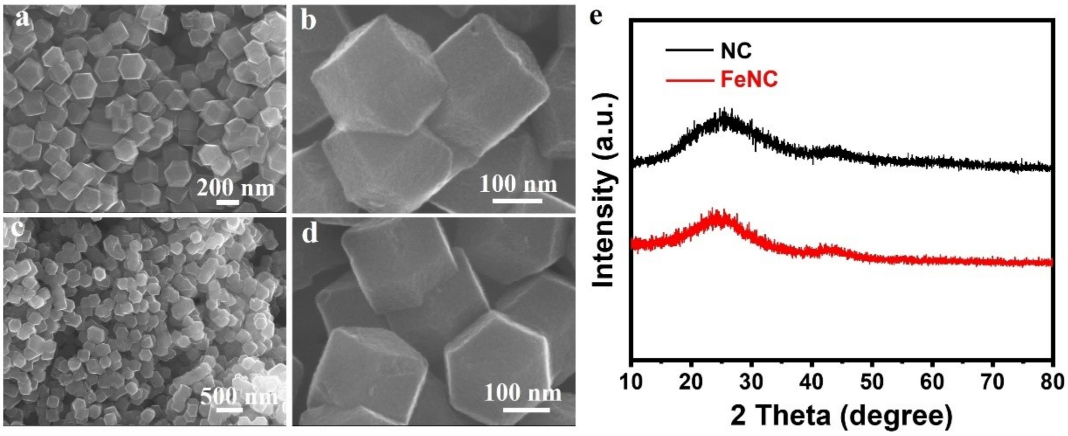

Figure S3. (a, b) SEM images of NC, (c, d) SEM images of FeNC, (c) XRD patterns of NC and FeNC.

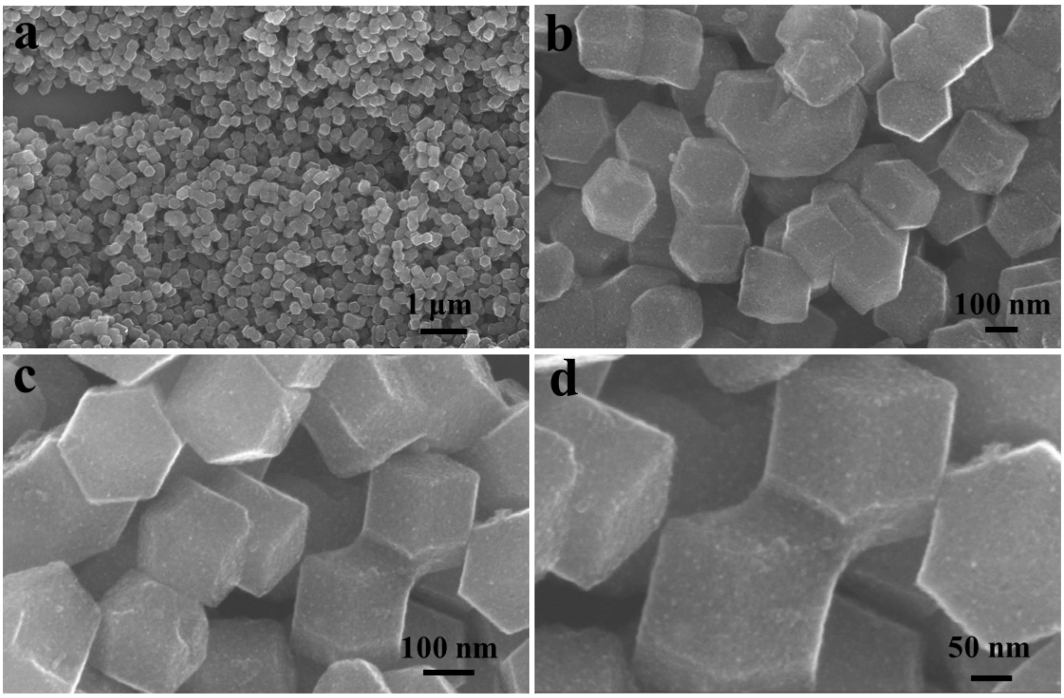

Figure S4. SEM images of O-PtCo-FeNC at different magnifications.

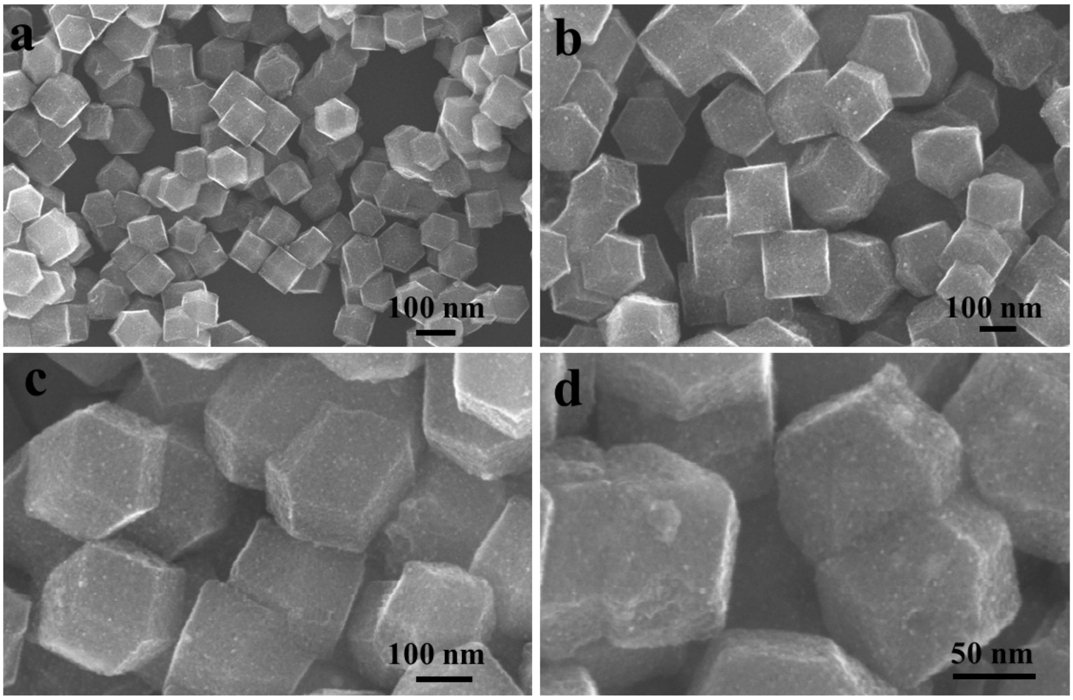

Figure S5. (a-d) SEM images of O-PtCo-NC at different magnifications.

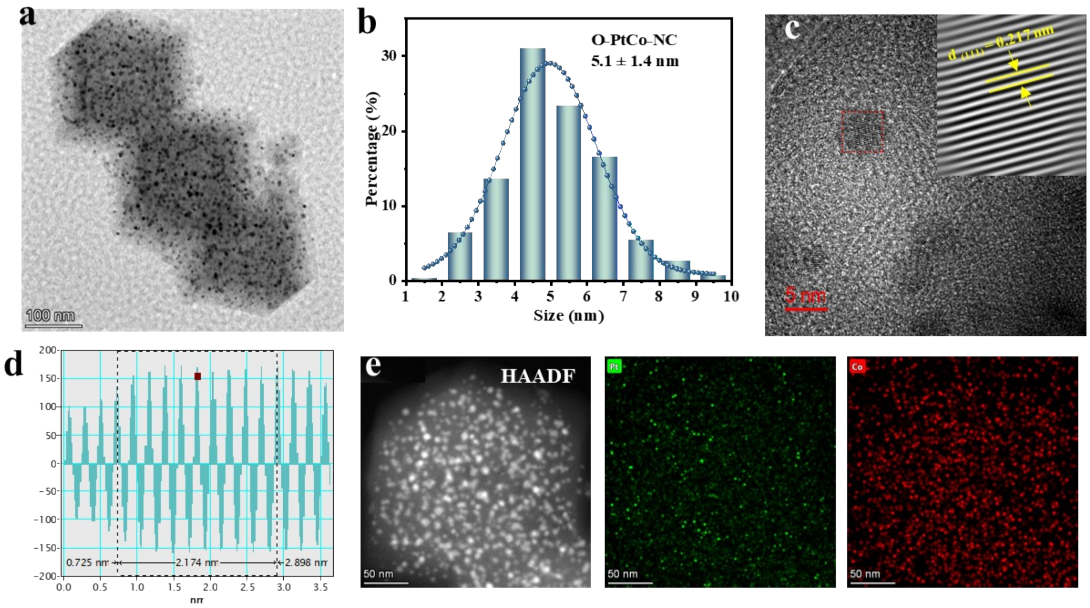

Figure S6. (a) TEM images of O-PtCo-NC, (b) histogram of particle diameters of O-PtCo-NC which we calculated from more than 200 particles, (c) HRTEM images and (d) corresponding lattice spacing bar plot of O-PtCo-NC, (e) HAADF-STEM image and EDS mapping (Pt, Co).

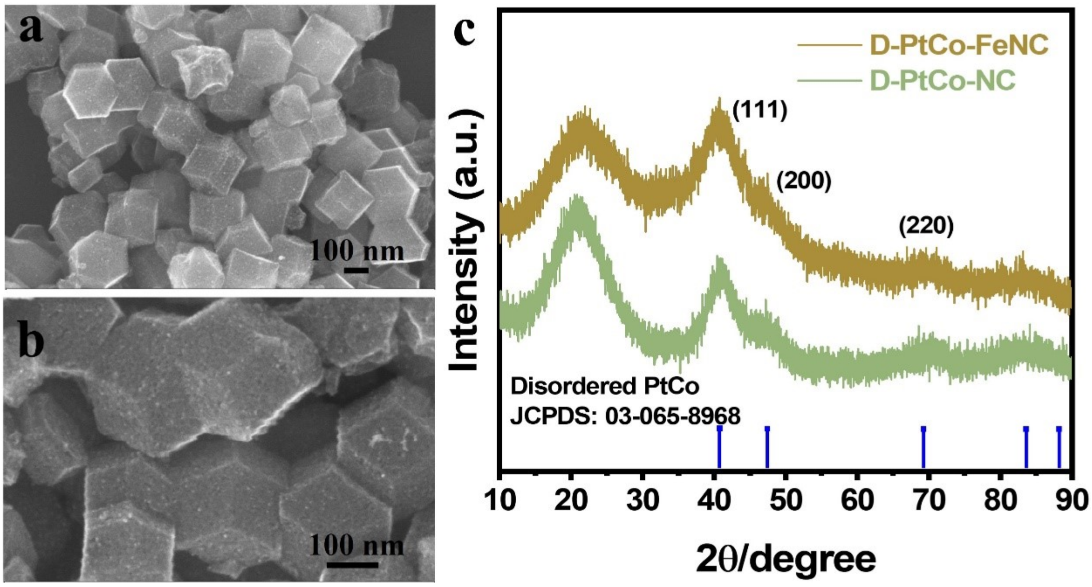

Figure S7. (a) SEM images of D-PtCo-NC, (b) SEM images of SEM images of D-PtCo-FeNC, (c) XRD pattern of D-PtCo-NC and D-PtCo-FeNC.

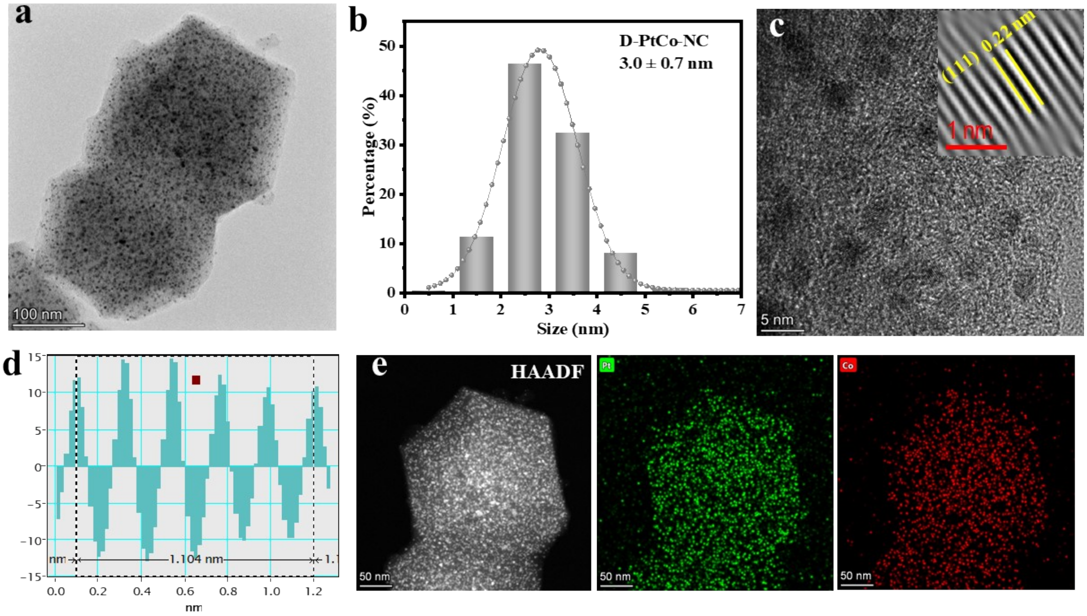

Figure S8. (a) TEM images of D-PtCo-NC, (b) histogram of particle diameters of D-PtCo-NC which we calculated from more than 200 particles, (c) HRTEM images and (d) corresponding lattice spacing bar plot of D-PtCo-NC, (e) HAADF-STEM image and EDS mapping (Pt, Co).

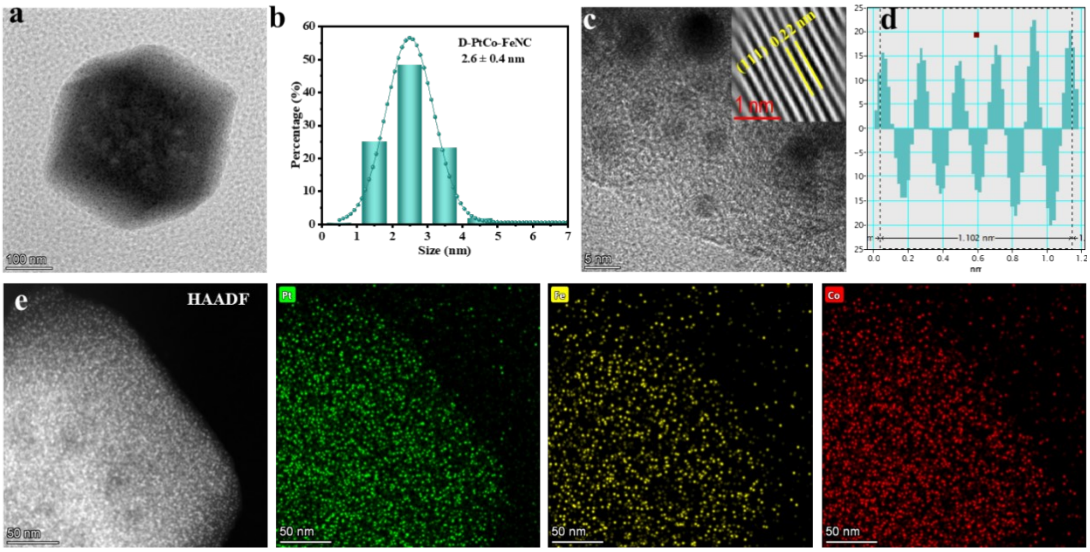

Figure S9. (a) TEM images of D-PtCo-FeNC, (b) histogram of particle diameters of D-PtCo-FeNC which we calculated from more than 200 particles, (c) HRTEM images and (d) corresponding lattice spacing bar plot of D-PtCo-FeNC, (e) HAADF-STEM image and EDS mapping (Pt, Fe, Co).

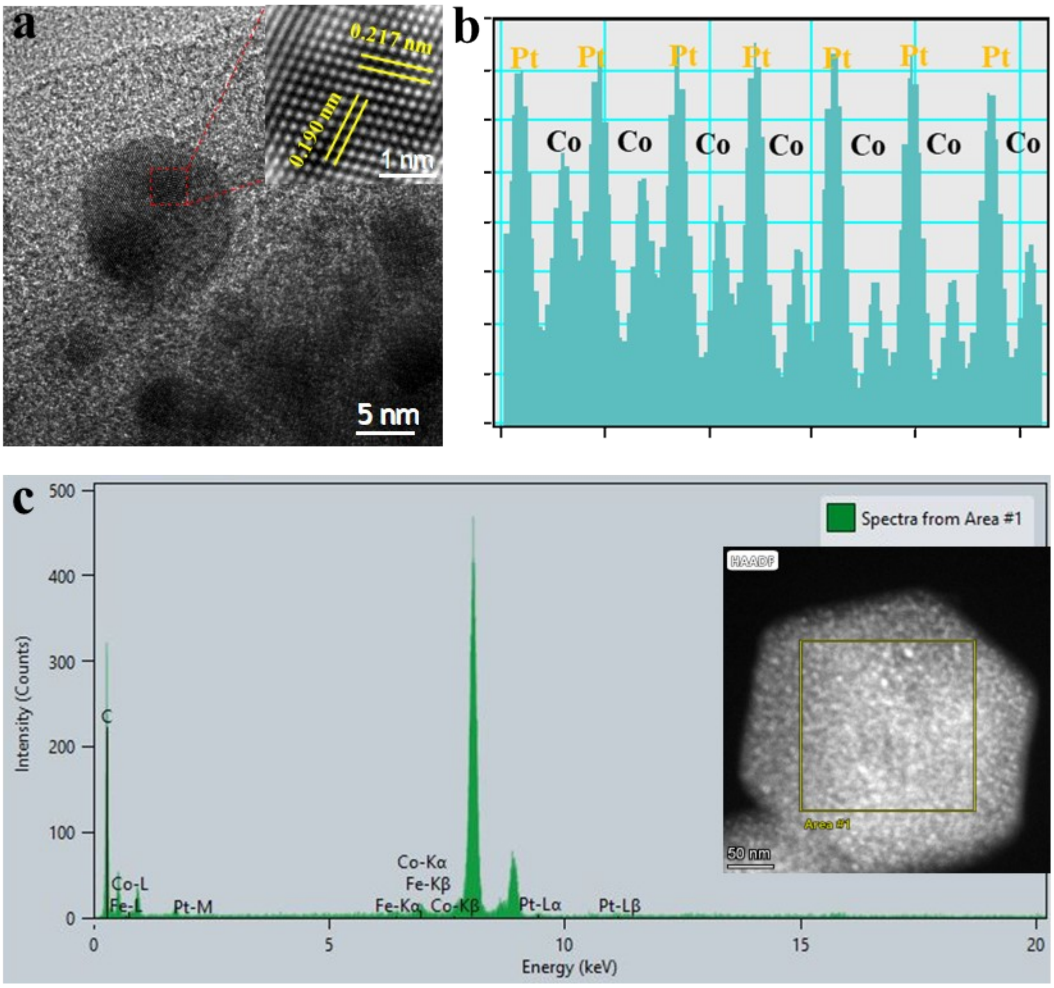

Figure S10. (a) HRTEM images of O-PtCo-FeNC, (b) lattice spacing bar plot of D-PtCo-FeNC, (c) selected area EDX spectrum.

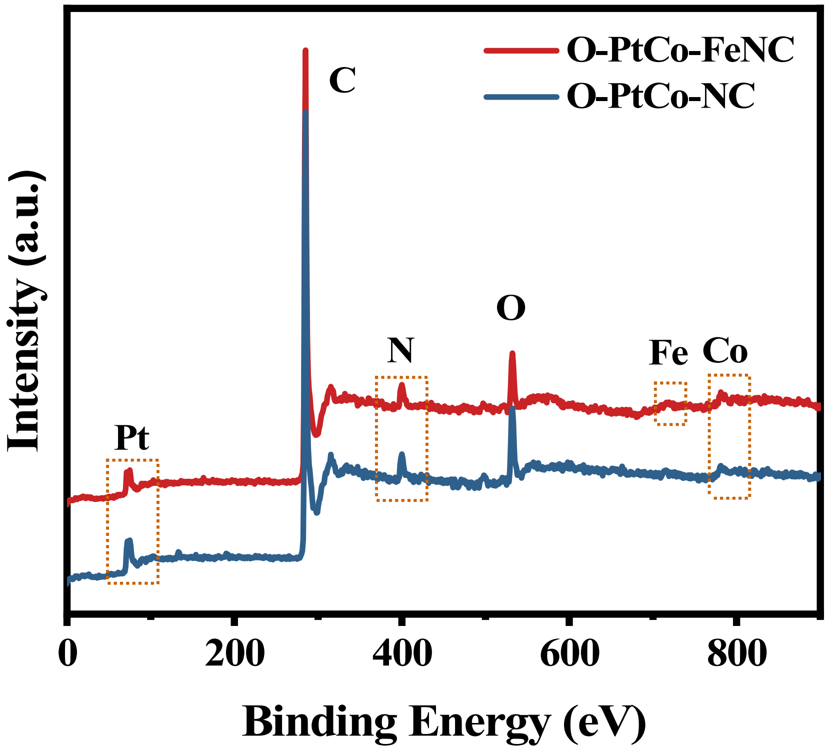

Figure S11. XPS survey of O-PtCo-NC and O-PtCo-FeNC.

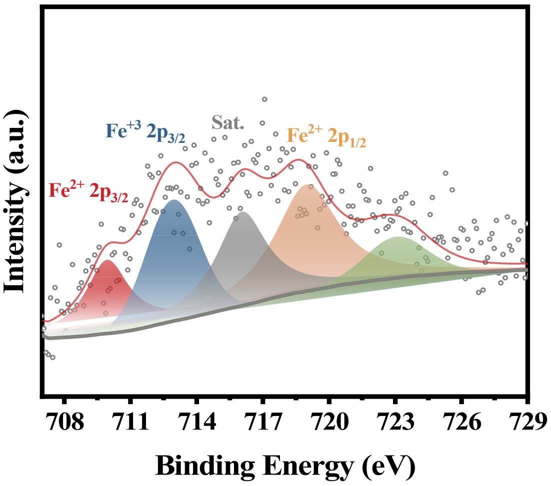

Figure S12. Fe XPS spectra of O-PtCo-FeNC.

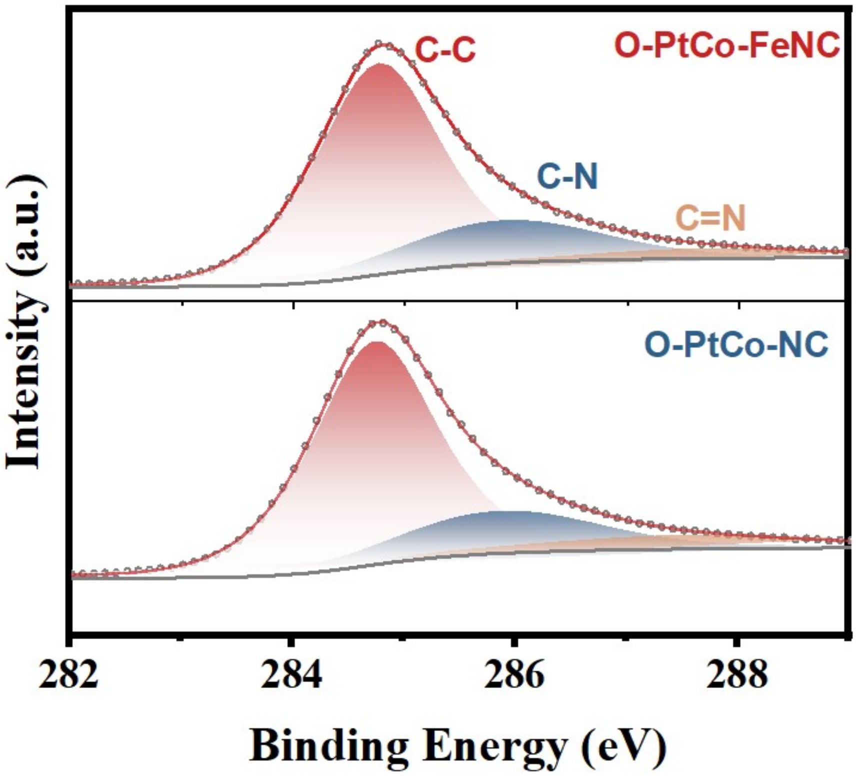

Figure S13. XPS spectrum comparison of the C 1s core-level among O-PtCo-NC and O-PtCo-FeNC catalysts.

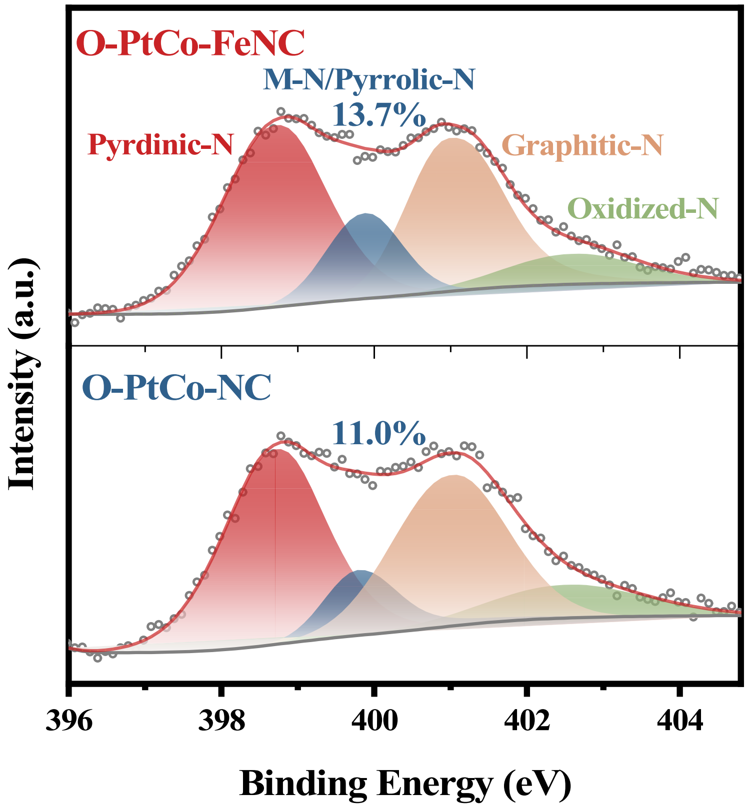

Figure S14. XPS spectrum comparison of the N 1s core-level among O-PtCo-NC and O-PtCo-FeNC catalysts.

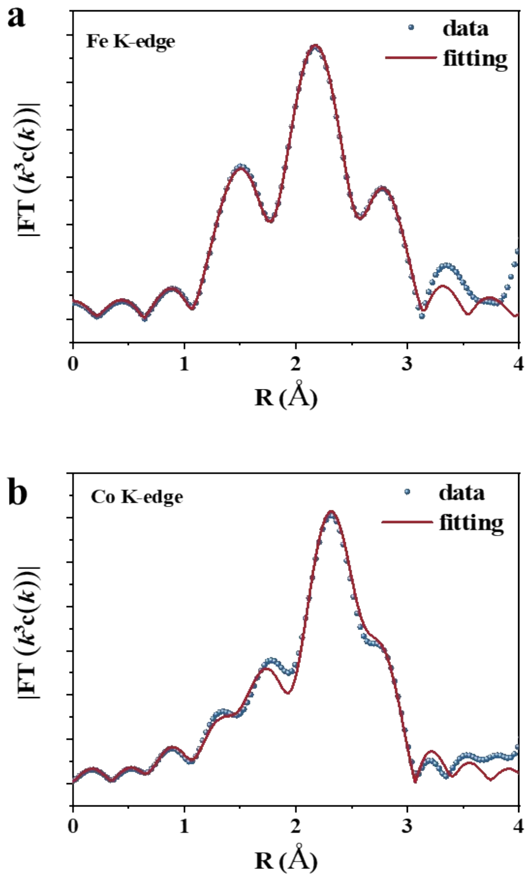

Figure S15. The applied scattering paths of Fe (a) and Co (b) K-edge for O-PtCo-FeNC.

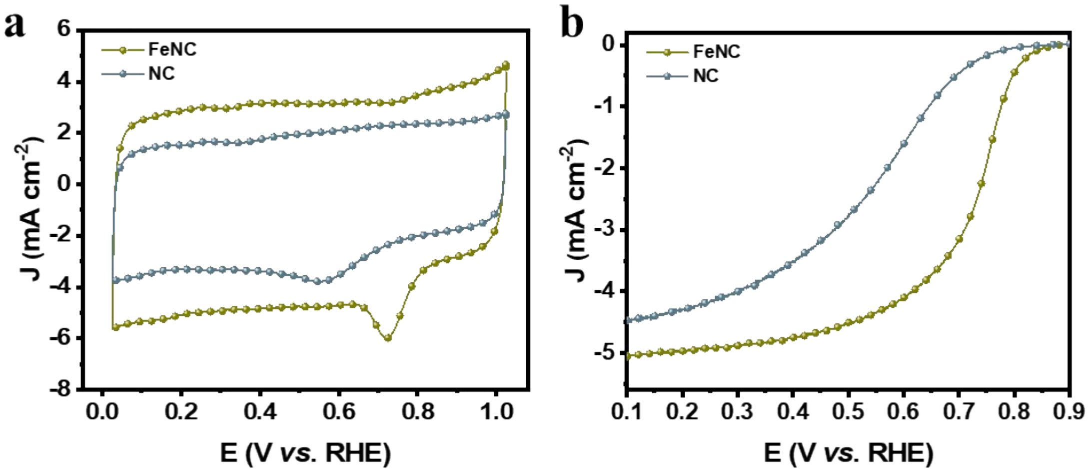

Figure S16. (a) CV and (b) LSV curves of NC and FeNC in O_2 saturated 0.5 M H_2SO_4 solution.

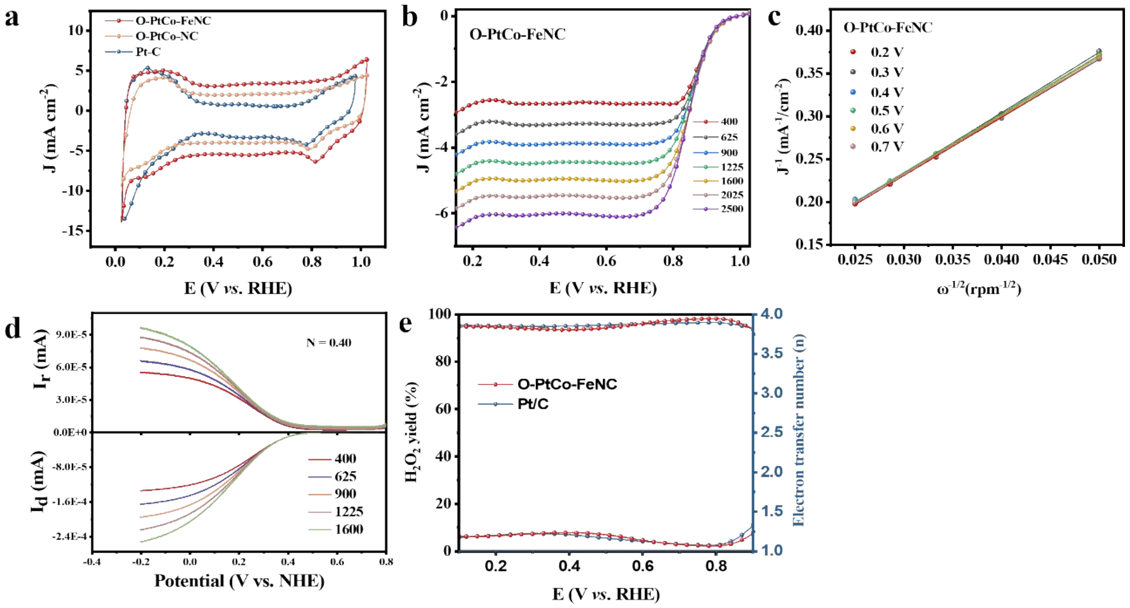

Figure S17. (a) CV curves of Pt/C, O-PtCo-NC and O-PtCo-FeNC, (b, c) LSV curves at different speeds and K-L plots of O-PtCo-FeNC, (d) RRDE polarization curves at different rotation speeds in 5 mM $k_3[Fe(CN)_6]$+100 mM KCl electrolyte, with a scan rate of 10 mv s^{-1}, (e) peroxide yield and electron transfer number of O-PtCo-FeNC and Pt/C at various potentials.

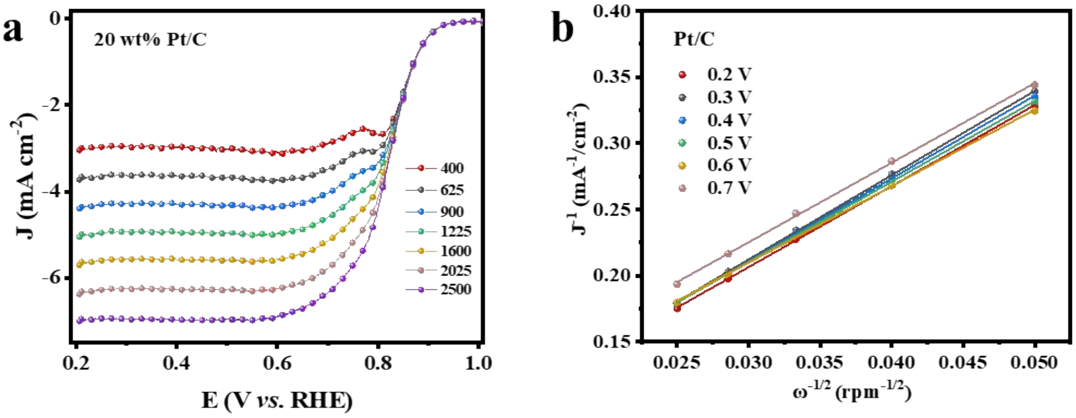

Figure S18. (a) LSV curves at different speeds and (b) K–L plots of Pt/C.

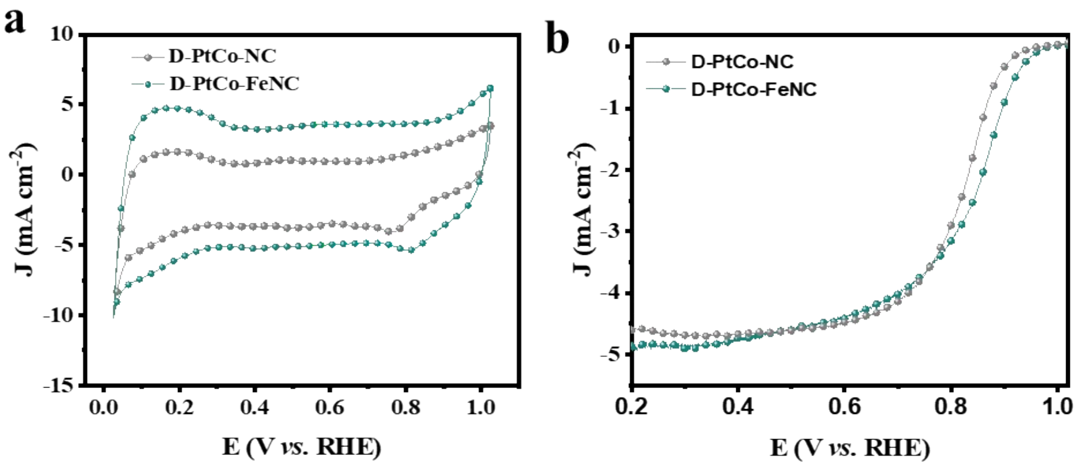

Figure S19. (a) CV and (b) LSV curves of D-PtCo-NC and D-PtCo-FeNC catalysts in O_2 saturated 0.5 M H_2SO_4 solution.

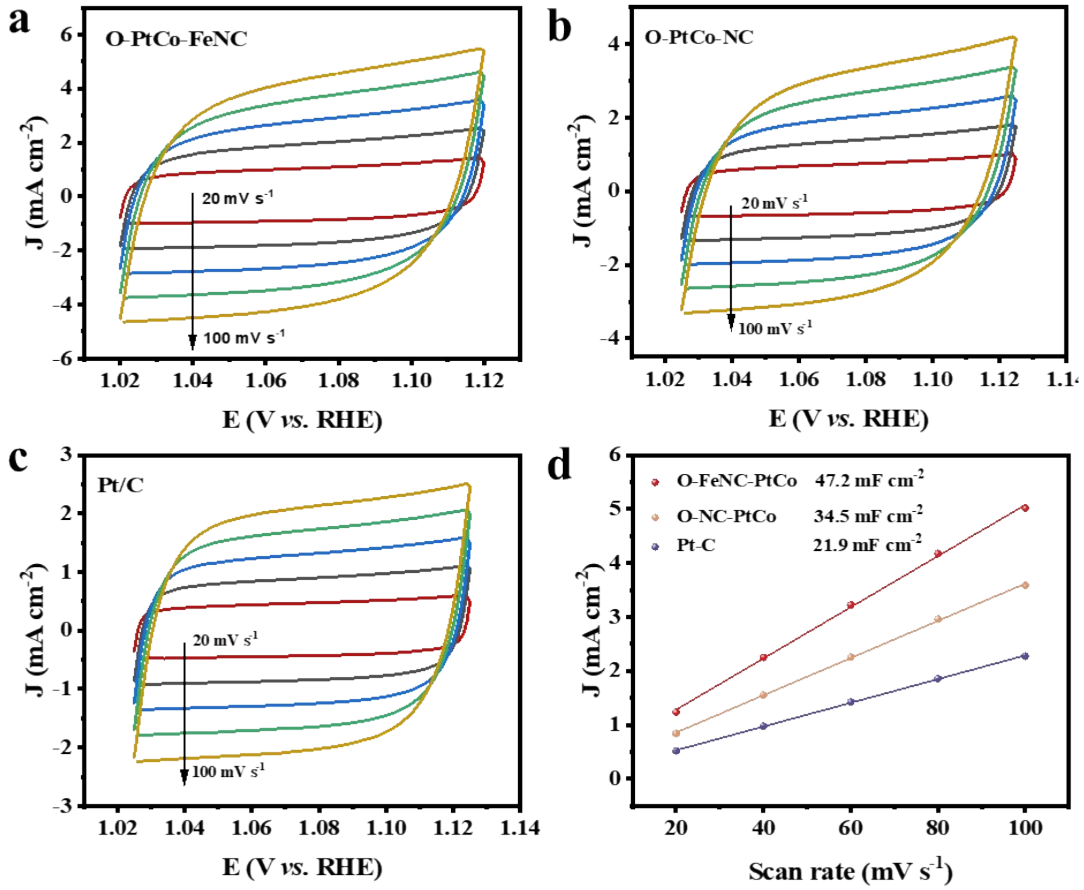

Figure S20. Double layer capacitance curve of O-PtCo-FeNC, O-PtCo-NC and Pt/C.

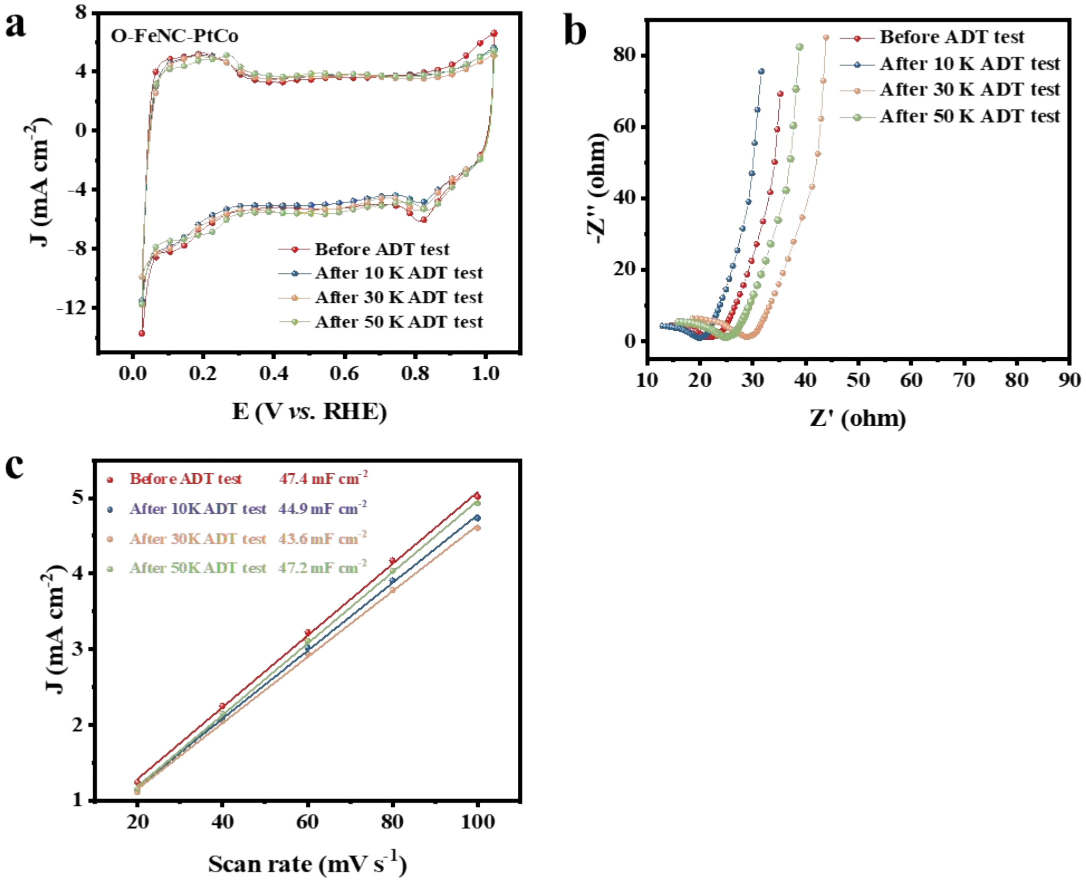

Figure S21. (a) CV curves, (b) electrochemical impedance test and (c) double layer capacitance curve of O-PtCo-FeNC catalysts before and after 50 k cycles ADT.

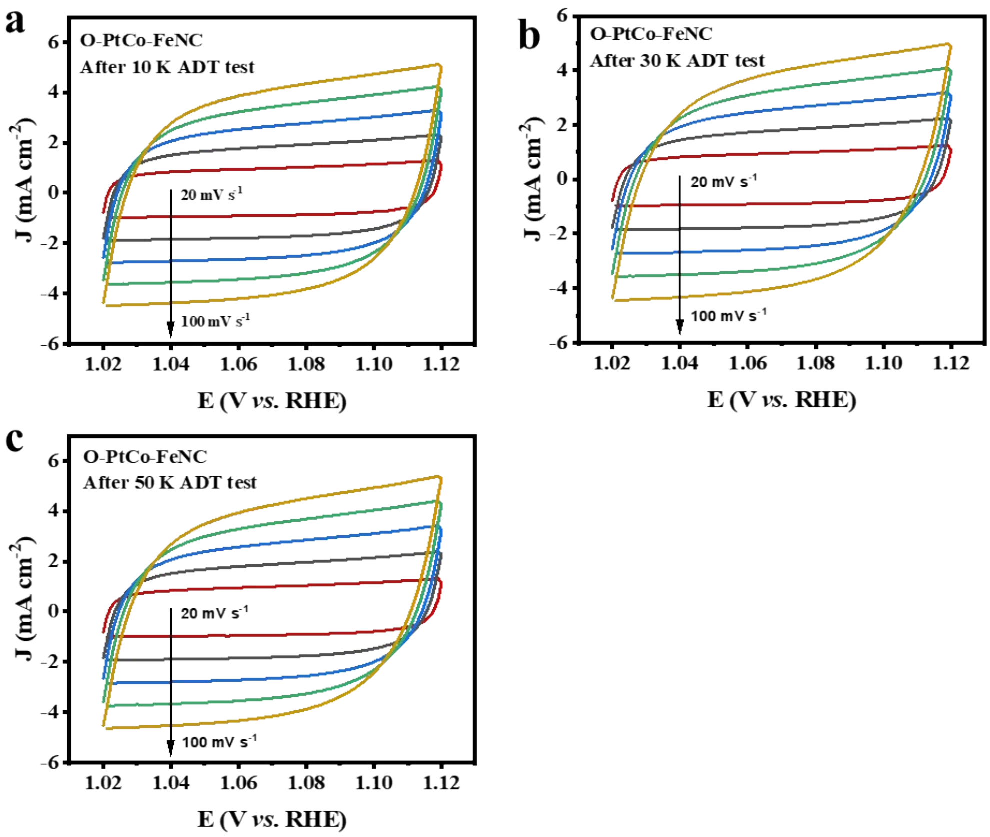

Figure S22. Double-layer CV curves of O-PtCo-FeNC during ADT test.

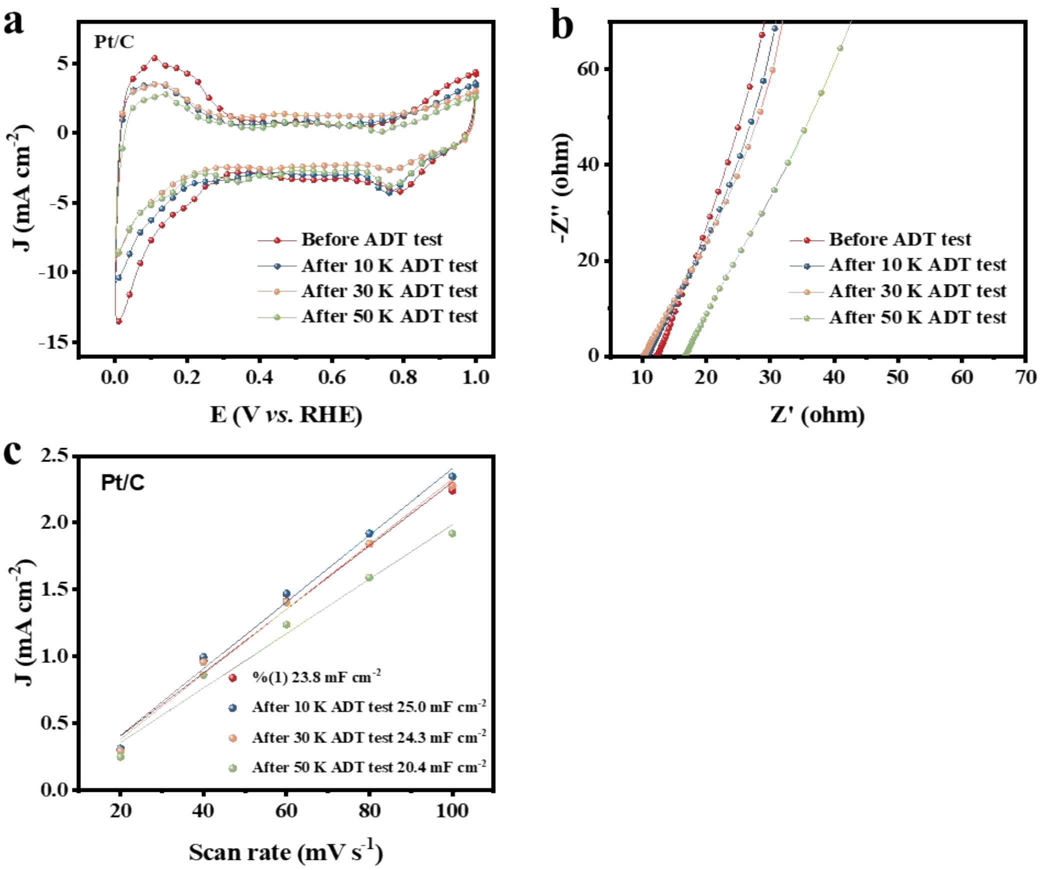

Figure S23. (a) CV curves, (b) electrochemical impedance test and (c) double layer capacitance curve of Pt/C catalysts before and after 50 k cycles ADT.

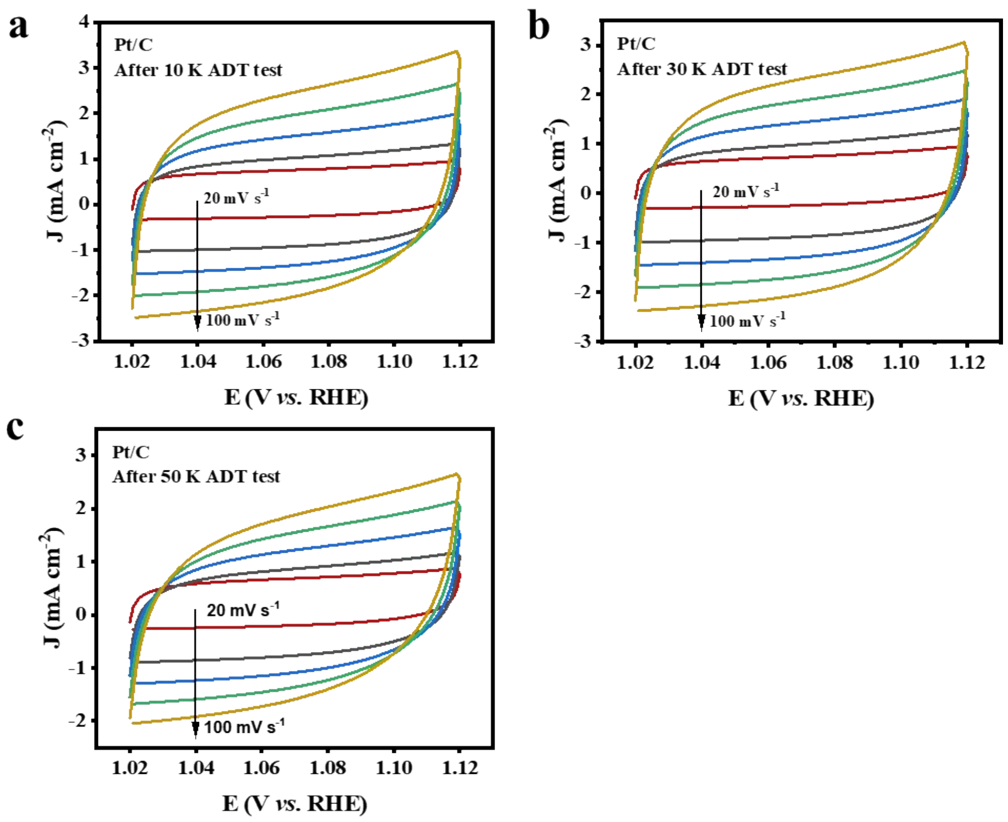

Figure S24. Double-layer CV curves of Pt/C during ADT test.

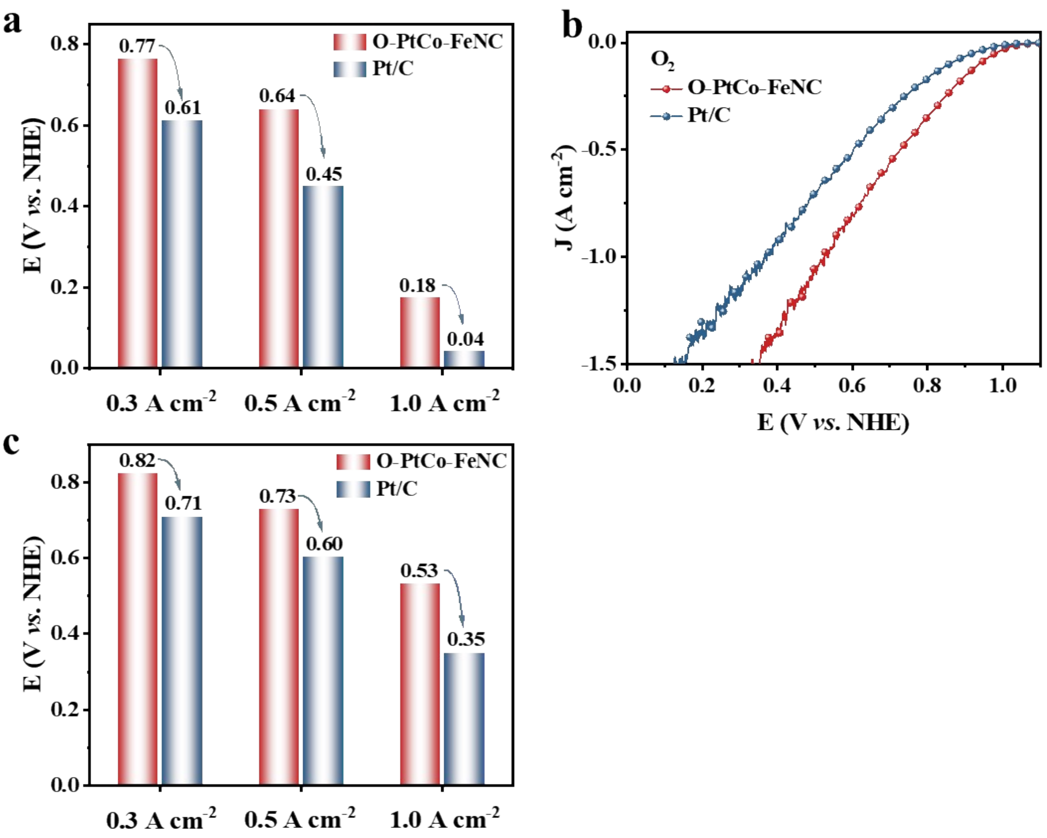

Figure S25. (a) Three-electrode tests of O-PtCo-FeNC and Pt/C based on GDE in air environment and the potentials required by the two catalysts at current densities of 0.3, 0.5, and 1.0 A cm^{-2}; (b, c) Three-electrode tests based on GDE in O_2 environment and the potentials required by the two catalysts at current densities of 0.3, 0.5, and 1.0 A cm^{-2}.

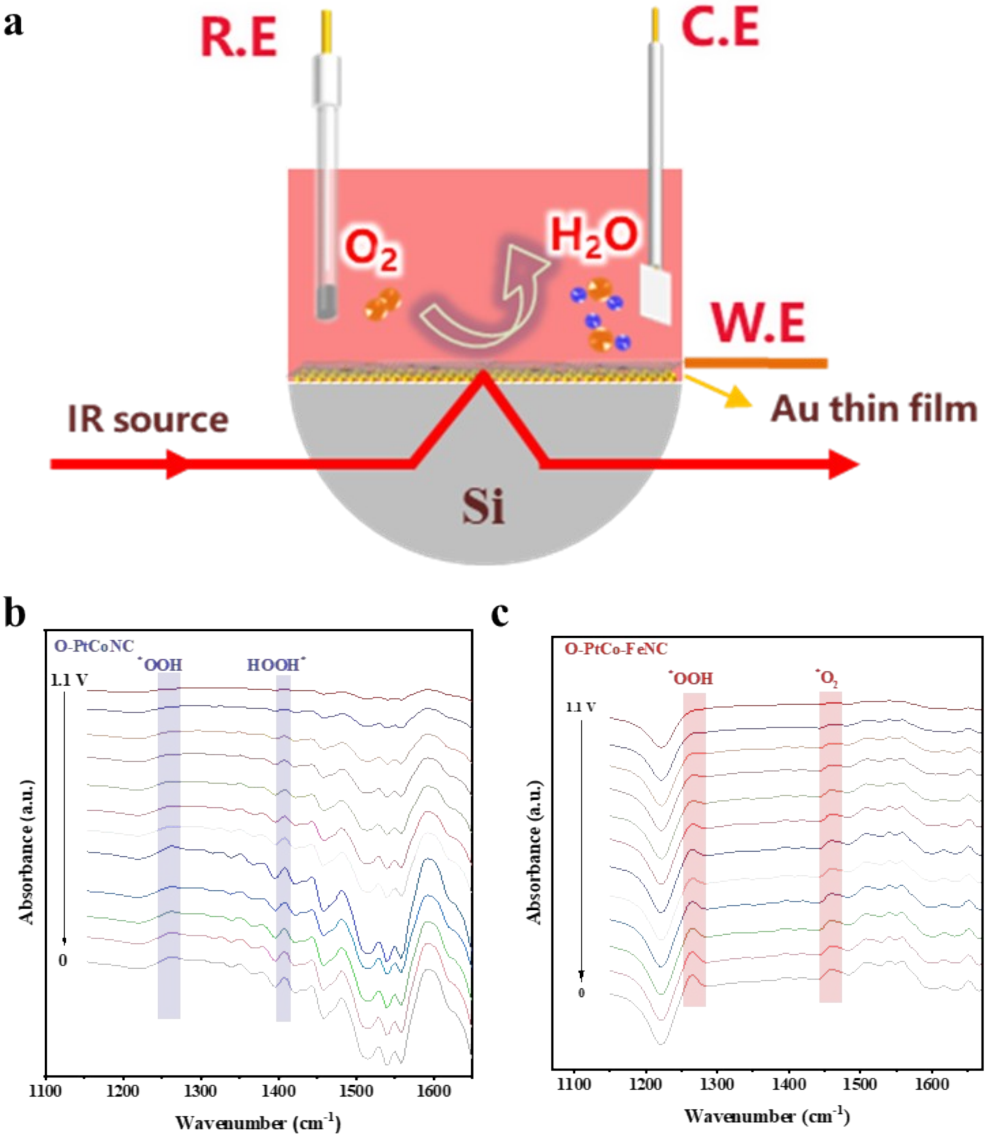

Figure S26. (a) Schematic diagram of electrochemical in-situ ATR-SEIRAS; (b, c) Electrochemical in-situ ATR-SEIRAS of O-PtCo-NC and O-PtCo-FeNC recorded at the different potentials in O_2-saturated 0.5 M H_2SO_4 solution.

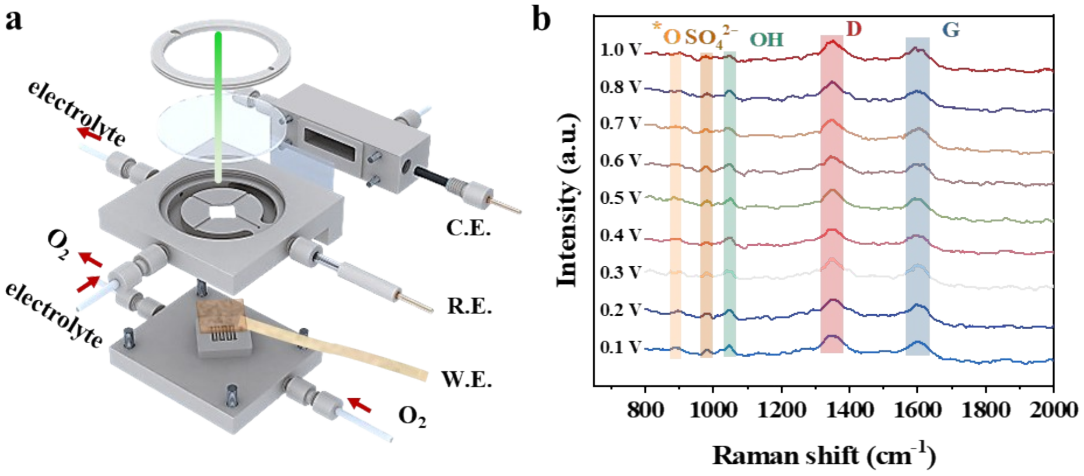

Figure S27. (a) Schematic diagram of electrochemical in-situ Raman test of ORR; (b) Raman spectral signal O-PtCo-FeNC at different potentials.

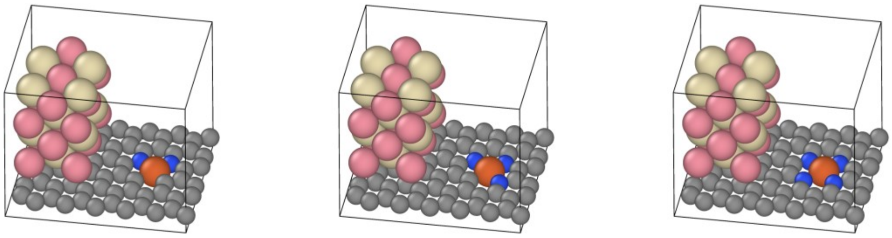

Figure S28. Structures to initialize FF.

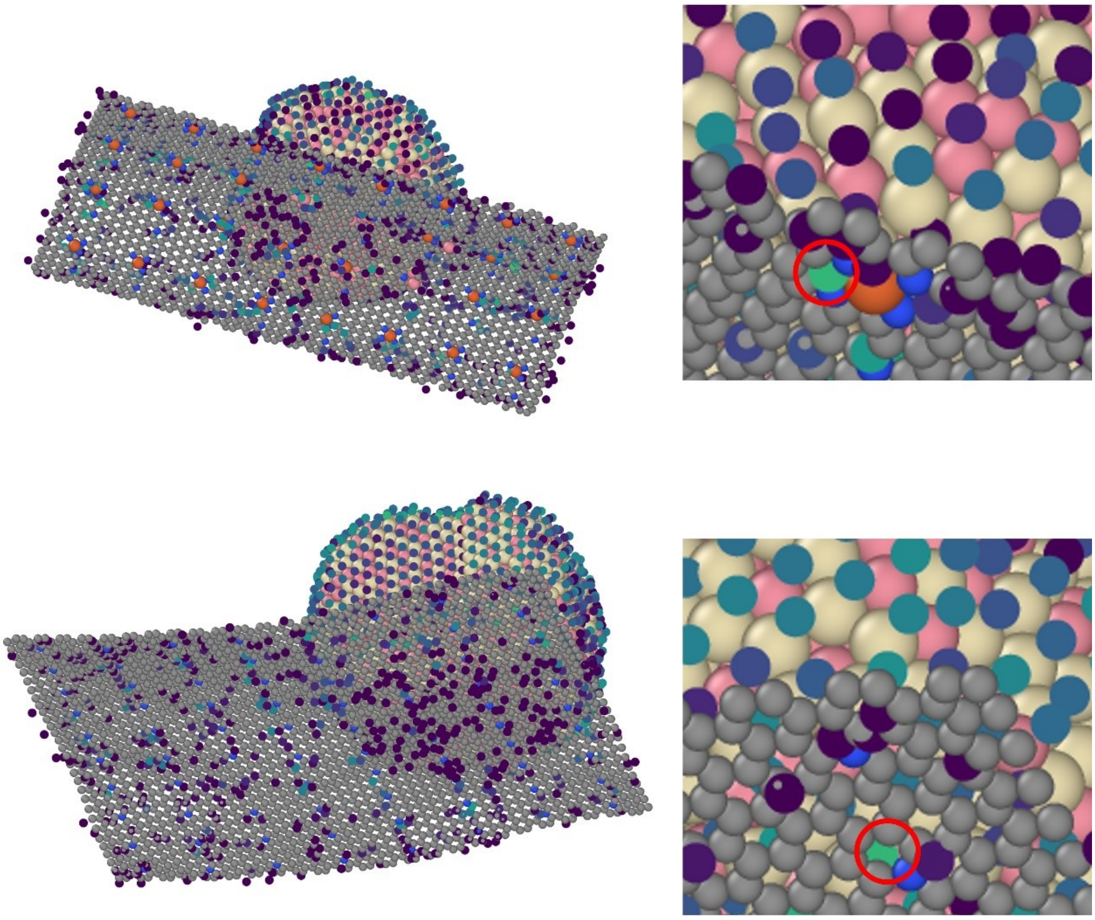

Figure S29. Representative snapshot of the MD process (reverse side).

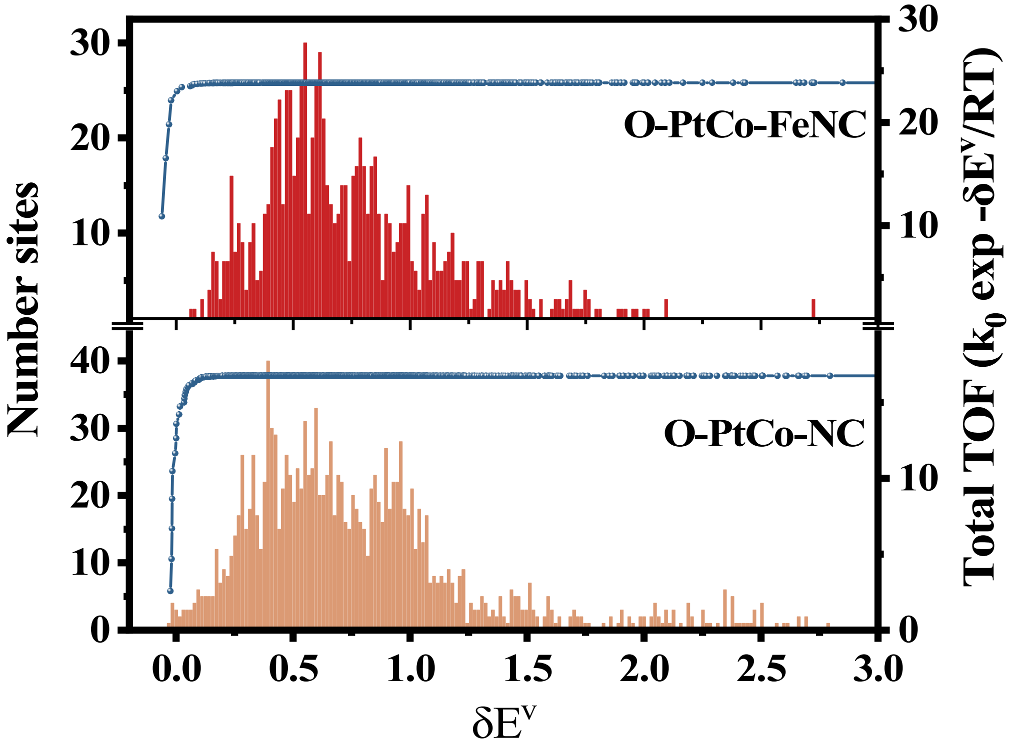

Figure S30. The distribution of δE^v value on each model. The blue lines are the integral lines summed from the most active sites (e.g., smallest δE^v) to the most inactive sites. Its associated values are given in the right axis.

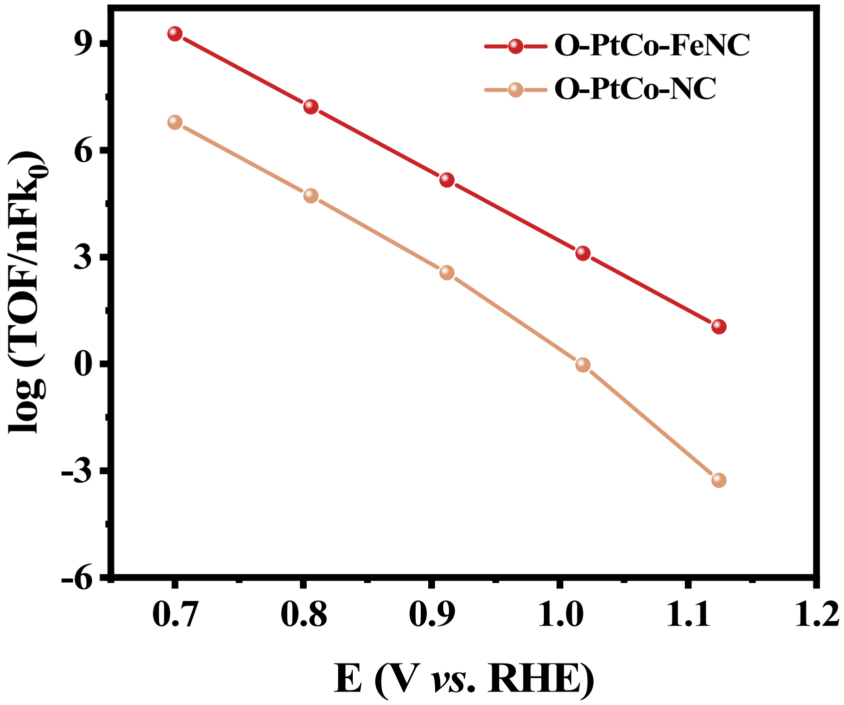

Figure S31. The Tafel curves in the range of 0.7 - 1.12 V were simulated and calculated.

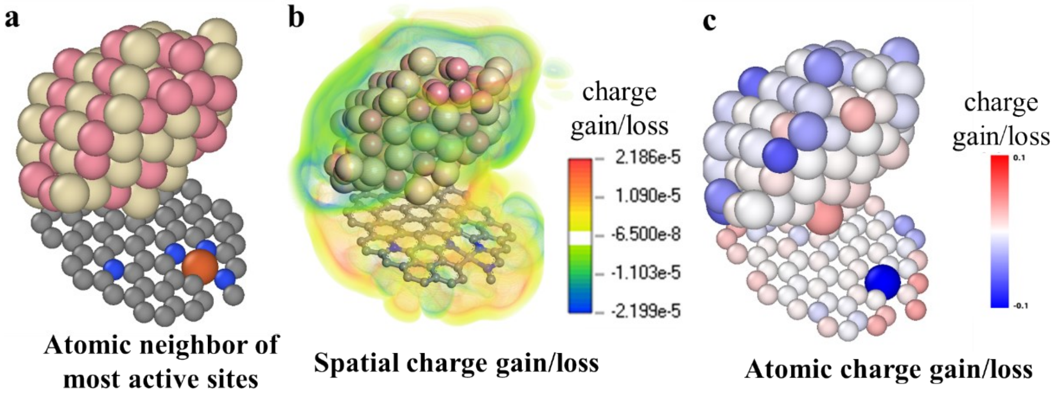

Fig. S32. The calculation results of differential charge density. (a) The atoms near the reaction center; (b) Spatial charge gain/loss; (c) Atomic charge gain/loss. The calculation method is rho(PtCo-FeN_3) - rho(PtCo) - rho(FeN_3). Therefore, positive values indicate electron gain and negative values indicate electron loss.

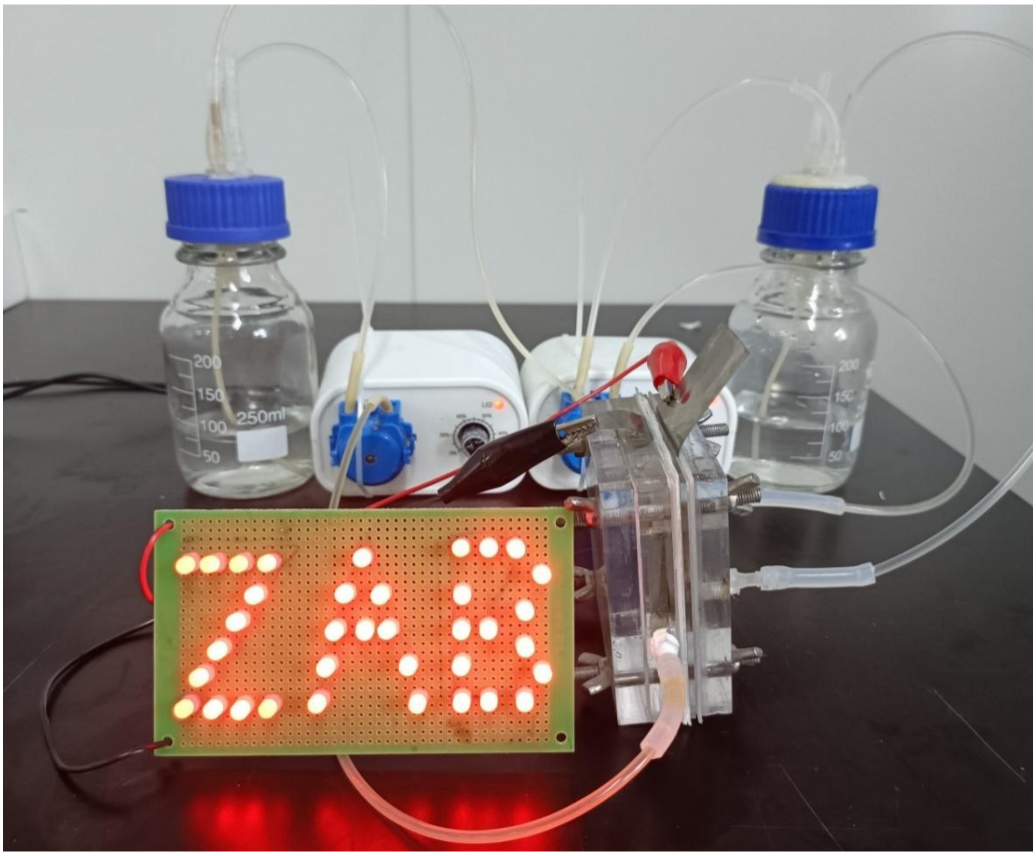

Figure S33. The digital pictures of LED arrays powered by our HZAB device.

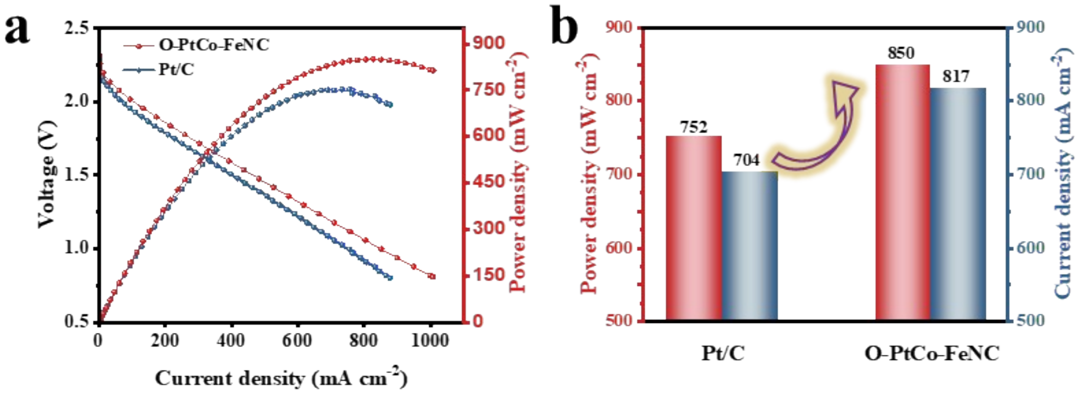

Figure S34. (a) Discharge polarization curve and power density of hybrid battery device; (b) Comparison diagram of maximum power density and corresponding current density of two batteries in oxygen condition.

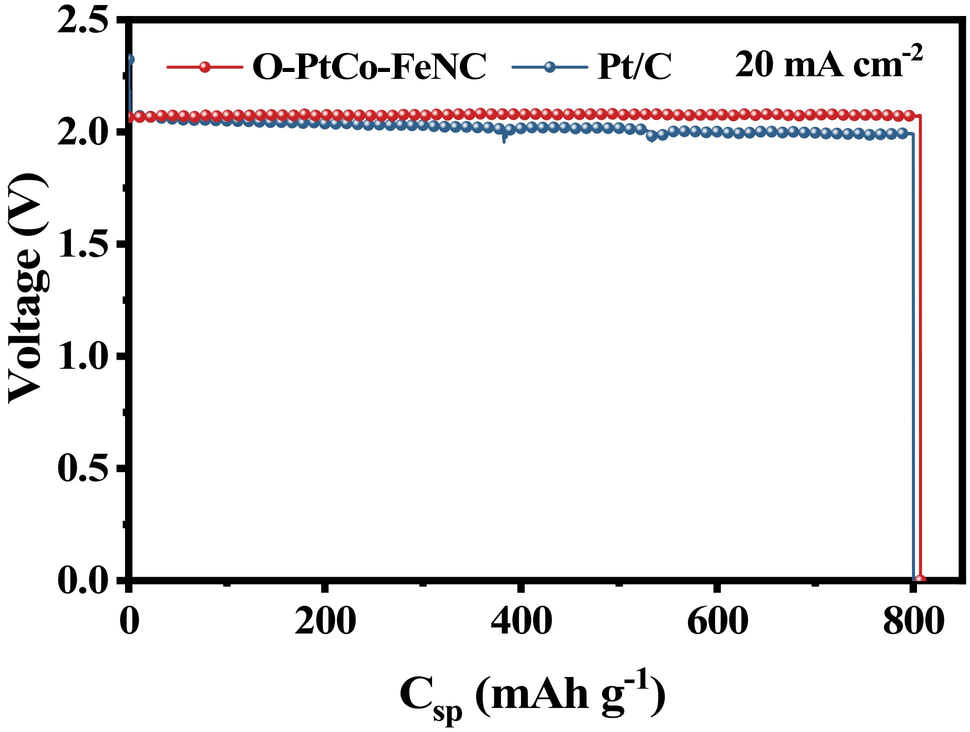

Figure S35. Mass-capacity inset for batteries equipped with O-PtCo-FeNC and Pt/C at 20 mA cm^{-2}.

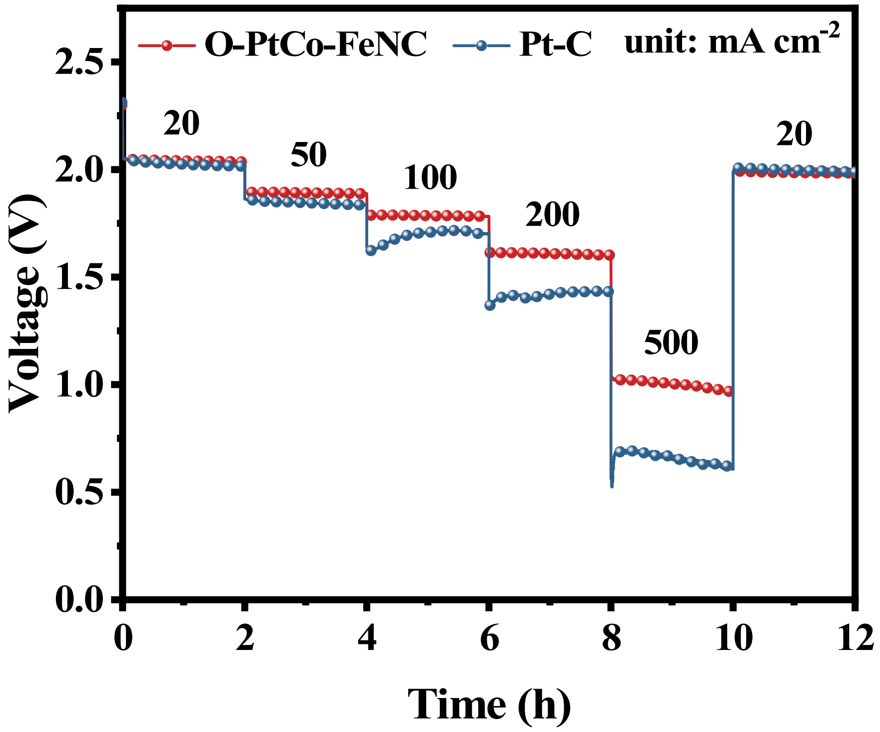

Figure S36. Galvanostatic discharge of the two batteries at different current density.

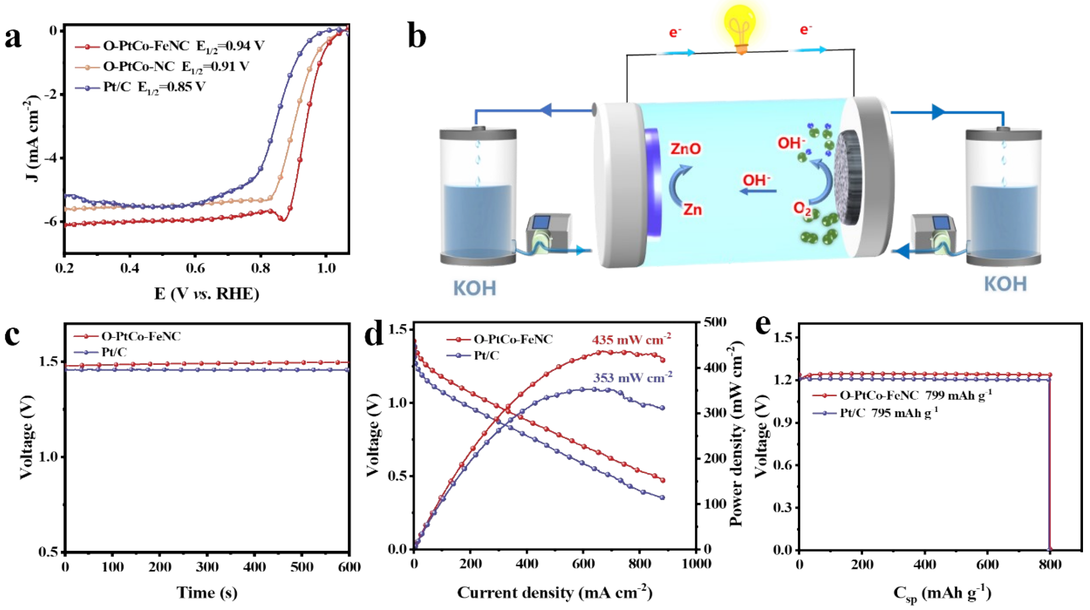

Figure S37. (a) ORR polarization curves of O-PtCo-FeNC, O-PtCo-NC and Pt/C in 0.1 M KOH; (b) Schematic diagram of alkaline Zn-air battery; (c) Open circuit voltage, (d) power density and (e) energy density curves of alkaline Zn-air batteries assembled with O-PtCo-NC and Pt/C as cathode catalysts, respectively.

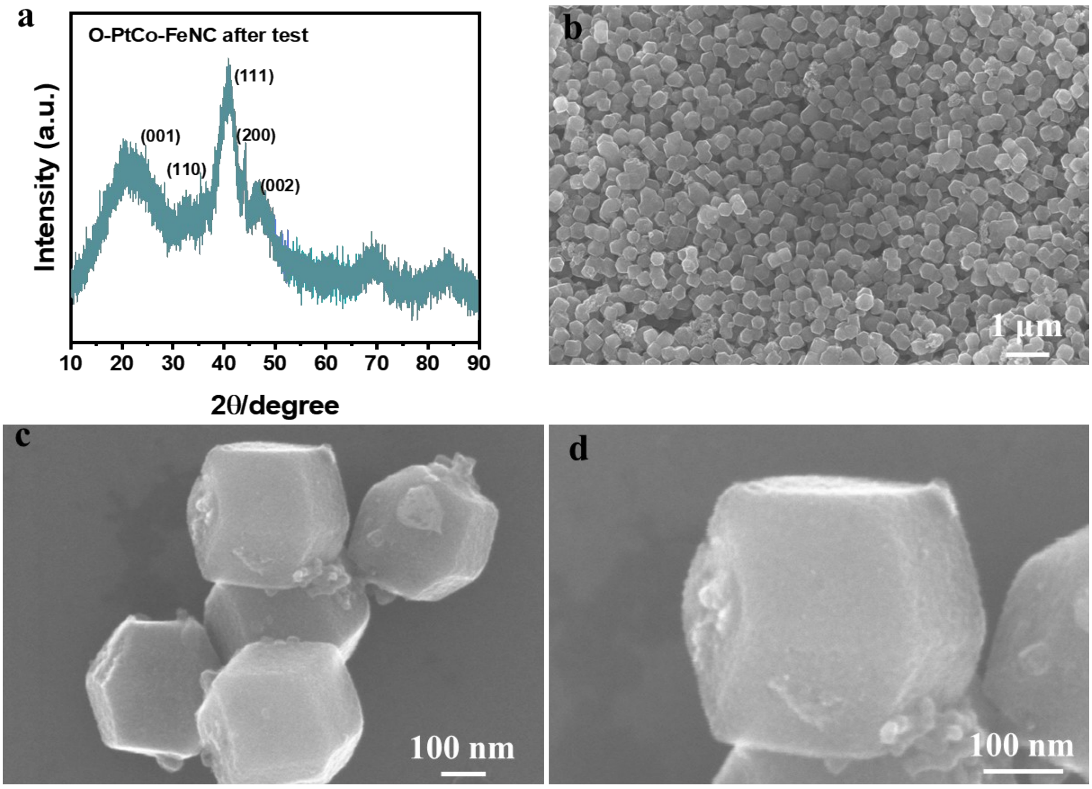

Figure S38. (a) XRD pattern and (b-d) SEM images of O-PtCo-FeNC at different magnifications after discharge test.

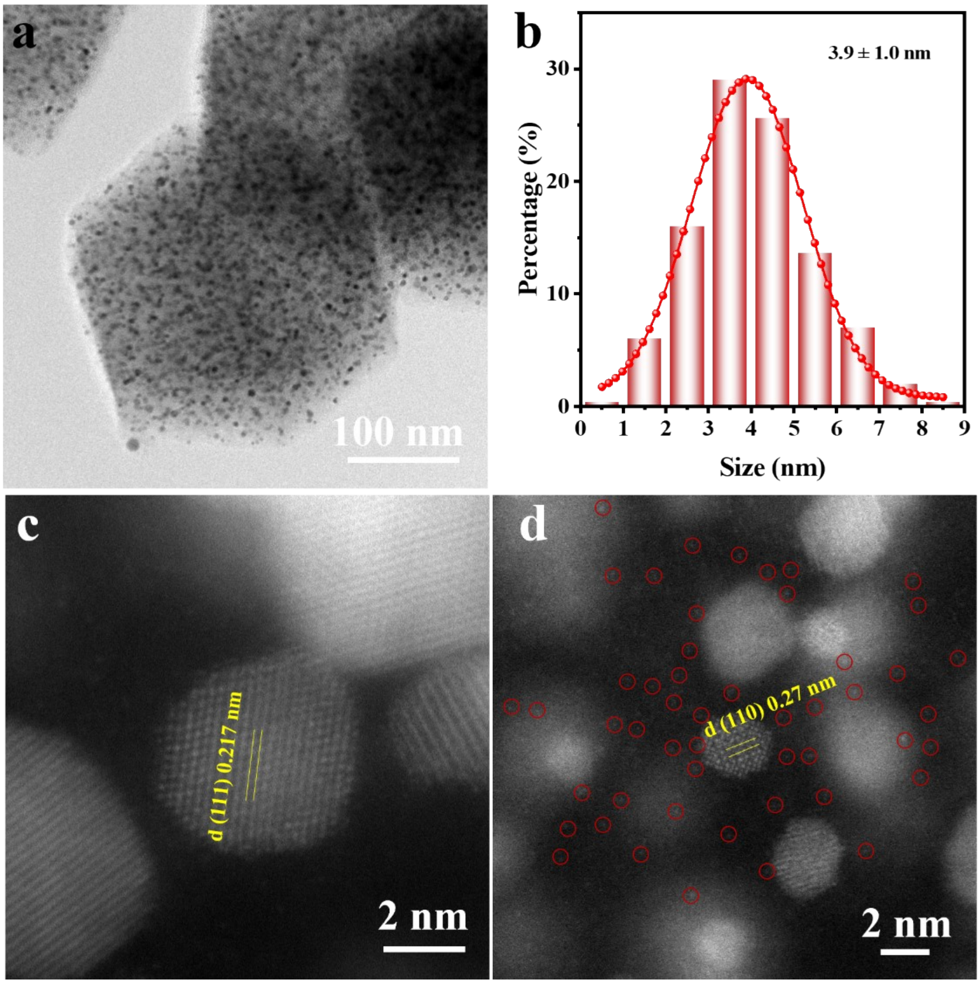

Figure S39. (a, b) TEM image of O-PtCo-FeNC after discharge and its particle size statistical histogram; (d, e) Aberration-corrected HAADF-STEM images of O-PtCo-FeNC after testing.

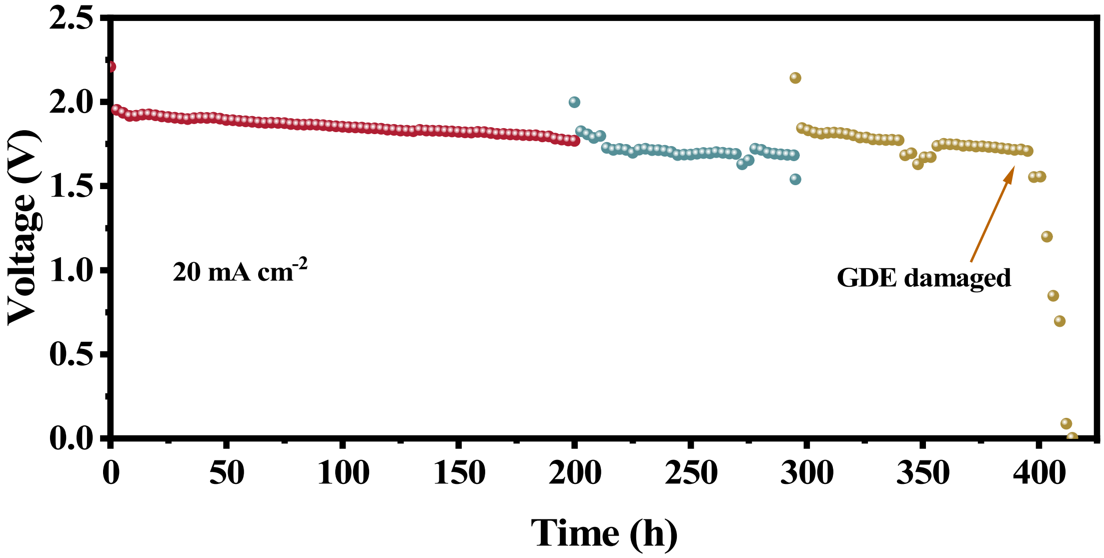

Figure S40. Battery discharge stability test at 20 mA cm^{-2}.

Table S1. Fitting parameters of Fe K-edge EXAFS.

Sample	Shell	*CN*[a]	*R*(Å)[b]	σ^2(Å^2)[c]	Δ*E*$_0$(eV)[d]	*R* factor
Fe foil	Fe-Fe1	8.0*	2.48	0.00495	8.05	0.0108
	Fe-Fe2	6.0*	2.86	0.00754	8.05	
	Fe-Fe3	12.0*	4.05	0.00910	-1.74	
O-PtCo-FeNC	Fe-N	2.8	1.922	0.00906	-1.819	0.0046
	Fe-Pt	5.1	2.611	0.01084	1.396	
	Fe-Co/Fe	1.8	2.616	0.01084	1.876	

Table S2. Fitting parameters of Co K-edge EXAFS.

Sample	Shell	*CN*[a]	*R*(Å)[b]	σ^2(Å^2)[c]	Δ*E*$_0$(eV)[d]	*R* factor
Co foil	Co-Co1	12*	2.495	0.00637	7.716	0.0078
	Co-Co2	6*	3.491	0.01114	7.716	
O-PtCo-FeNC	Co-N	1.9	2.004	0.0107	8.629	0.0052
	Co-Co/Fe	1.5	2.606	0.00831	5.251	
	Co-Pt	3.9	2.635	0.00796	5.251	

[a]*CN*, coordination number; [b]*R*, the distance to the neighboring atom; [c]σ^2, the Mean Square Relative Displacement (MSRD); [d]ΔE_0, inner potential correction; *R* factor indicates the goodness of the fit. $S0^2$ was fixed to 0.767, according to the experimental EXAFS fit of Fe foil by fixing *CN* as the known crystallographic value. * This value was fixed during EXAFS fitting, based on the known structure of Fe foil. Error bounds (accuracies) that characterize the structural parameters obtained by EXAFS spectroscopy were estimated as C*N* ± 20%; *R* ± 1%; σ^2 ± 20%; ΔE_0 ± 20%. Fitting range: $2.0 \leq k$ (/Å) ≤ 12.0.

Table S3. Performance comparison between O-PtCo-FeNC and other recently reported catalysts.

Catalysts	Pt loading (wt%)	$E_{1/2}$ (V) in H_2SO_4	M_A (A mg_{Pt}^{-1})	S_A (mA cm^{-1})	Cycle number@$E_{1/2}$ loss	Ref.
Pt SAs/$CoPt_3$@NC	3.2	0.928 in $HClO_4$	1.323@0.9 V	/	30000@2	13
Pt/HFe_{SA}–HCS	3.46	0.91 in $HClO_4$	0.98@0.9 V	1.39 mA cm_{Pt}^{-2}	20000@11	14
Pt_3Co/FeN_4–C	20	0.95 in $HClO_4$	1.34@0.9 v	3.98 mA cm_{Pt}^{-2}	30000@30	15
Pt_A@FeSA-N-C	13.1	0.923 in $HClO_4$	~0.87@0.9 V	1.35 mA cm_{Pt}^{-2}	5000@7	16
Pt@Co SAs-ZIF-NC	5.01	0.919 in $HClO_4$	0.48@0.9 V	0.64 mA cm^{-2}	5000@21	17
PtCo	7.3	/	0.041@0.9 V	0.30 mA cm^{-2}	/	18
Pt_3Co/C-700	20	0.945 in $HClO_4$	0.52@0.9 V	1.1 mA cm_{Pt}^{-2}	5000@10	19
Pt-Fe-N-C	1.7	~0.85 in $HClO_4$	/	/	40000@14	20
PtCo@NGNS	12.2	0.95 in $HClO_4$	1.29@0.9 V	1.70 mA cm_{Pt}^{-2}	30000@20	21
PtCoNi@NC NTs	3.3	0.97 in $HClO_4$	3.46@0.9 V	4.61 mA cm_{Pt}^{-2}	10000@10	22
$PtCo_3$-H600	15	0.903 in $HClO_4$	0.740@0.9 V	/	30000@5	23
LP@PF-2	2.82	0.959 in $HClO_4$	12.36@0.9 V	/	/	24
PtFe/Fe-N-C	7.16	0.93 in $HClO_4$	1.48@0.9 V	/	50000@7	25
Pt_1Fe_1 @ $Fe_{0.5}$ NC-900	6.13	0.889 in $HClO_4$	1.157@0.85 V	/	30000@21	26
$Pt_{56}Mn_{44}$/C	18	0.910 in $HClO_4$	0.53@0.9 V	1.0 mA cm_{Pt}^{-2}	80000@20	27

Catalysts	Pt loading (wt%)	$E_{1/2}$ (V) in H_2SO_4	M_A (A mg_{Pt}^{-1})	S_A (mA cm^{-1})	Cycle number@$E_{1/2}$ loss	Ref.
Pt@Mn-SAs/N-C	1.98	0.896 in $HClO_4$	0.62@0.9 V	/	5000@1	28
CoZ-60Pt	15	0.942 in $HClO_4$	0.53@0.9 V	1.55	3000@15	29
PtZn-IMC@NC	12	0.847	0.808	1.29 mA cm_{Pt}^{-2}	20000@1	30
p-Pt@p-NCNT	7.85	0.697	/	/	/	31
PtCo/C-900	20	~0.79	0.084@0.9 V	2.8 mA cm_{Pt}^{-2}	/	32
20 wt% Pt/C	20	0.81	0.159@0.85 V	0.40	50000@50	This work
O-PtCo-FeNC	8.9	0.86	1.34@0.85 V	0.93	50000@8	This work

Table S4. Performance comparison between O-PtCo-FeNC and other recently reported catalysts.

Catalysts	$E_{1/2}$ (V) in 0.1 M KOH	OCP (V)	Peak power density (mW cm^{-2})	Energy density (Wh kg$^{-1}_{Zn}$)	Time (h)@discharge current density (mA cm^{-2})	Ref.
FeN4/NGO_2.5m	0.91	1.35	217	900	100 @10	[33]
Fe SAs/NC	0.93	1.461	306.1	100.1	315 @10	[34]
3D SAFe	0.90	1.47	156	1018	80 @10	[35]
OLC/Co-N-C	0.864	1.48	238	800	100 @2	[36]
FeCo-NCH	0.889	1.45	414.5	1009.1	100 h@5	[37]
FeMn-DSAC	0.922	1.45	184	888	218 cycles (80 h) @2	[38]
20 wt% Pt/C	0.76 (0.5 M H_2SO_4)	2.25	380	1522	150 @10	[39]
CoPOF@CNT	0.7	1.32	570	413 Wh L^{-1}	90 @2	[40]
Mn-RuO_2	0.862	1.55	181	~975	2500 h (15000 cycles)@10, 466.7 h (2800 cycles)@50, 300 h (1800 cycles)@100	[41]
Co_2Fe_1@NC	0.85	1.454	423.7	1011.5	250 @2	[42]
CuS/NiS_2	~0.72	1.44	172.4	1015.2	83 h (500 cycles)@ 25	[43]
FeCo@NC	0.78 (0.1 M $HClO_4$)	2.23	562.7	1498	300 @5	[44]
h-NNC-1150	0.77 (0.5 M H_2SO_4)	2.11	270	1279	150 @10	[45]

Catalysts	$E_{1/2}$ (V) in 0.1 M KOH	OCP (V)	Peak power density (mW cm^{-2})	Energy density (Wh kg^{-1}$_{Zn}$)	Time (h)@discharge current density (mA cm^{-2})	Ref.
Co_2B	0.83	1.45	500	1078	25 @10	[46]
FeP/Fe2O3@ NPCA	0.838	1.30	130	926	170 h (1020 cycles) @5, 126 h (756 cycles) @10	[47]
CoFe-S@3D-S-NCNT	0.855	1.55	223	1046	900 @5	[48]
Mn-Fe/p-DC-900	0.80 0.5 M H_2SO_4	2.2	375	1313	48 @100	[49]
20 wt% Pt/C	0.85 V	1.46	353	959	/	This work
O-PtCo-FeNC	0.94 V	1.50	435	994	/	This work
20 wt% Pt/C	0.81 0.5 M H_2SO_4	2.29	649	1600	/	This work
O-PtCo-FeNC	0.86 0.5 M H_2SO_4	2.32	751	1610	144 @300, 400 @20	This work

References

1. B. Ravel and M. Newville, *J. Synchrotron Radiat.* 2005, **12**, 537-541.
2. S. I. Zabinsky, J. J. Rehr, A. Ankudinov, R. C. Albers and M. J. Eller, *Phys. Rev. B* 1995, **52**, 2995-3009.
3. J. Behler and M. Parrinello, *Phys. Rev. Lett.* 2007, **98**, 146401.
4. Y. Zhang, H. Wang, W. Chen, J. Zeng, L. Zhang, H. Wang and W. E, *Comput. Phys. Commun.* 2020, **253**.
5. A. P. Thompson, H. M. Aktulga, R. Berger, D. S. Bolintineanu, W. M. Brown, P. S. Crozier, P. J. In't Veld, A. Kohlmeyer, S. G. Moore and T. D. Nguyen, *Comput. Phys. Commun.* 2022, **271**, 108171.
6. A. L. J. K. Nørskov; J. Rossmeisl, L. Lindqvist, J. R. Kitchin,T. Bligaard,H. Jo´nsson, *J. Phys. Chem. B* 2004, **2004**, 17886-17892.
7. L. Wang, Z. Gao, K. Su, N. T. Nguyen, R. T. Gao, J. Chen and L. Wang, *Adv. Funct. Mater.* 2024, 2403948.
8. B. H. Zhang D, Dai F Z, et al., *arXiv:2208.08236* 2022.
9. D. Zhang, X. Liu, X. Zhang, C. Zhang, C. Cai, H. Bi, Y. Du, X. Qin, J. Huang and B. Li, *arXiv preprint arXiv:2312.15492* 2023.
10. L. Chanussot, A. Das, S. Goyal, T. Lavril, M. Shuaibi, M. Riviere, K. Tran, J. Heras-Domingo, C. Ho and W. Hu, *Acs Catal.* 2021, **11**, 6059-6072.
11. S. Grimme, J. Antony, S. Ehrlich and H. Krieg, *J. Chem. Phys.* 2010, **132**.
12. P. Giannozzi, S. Baroni, N. Bonini, M. Calandra, R. Car, C. Cavazzoni, D. Ceresoli, G. L. Chiarotti, M. Cococcioni, I. Dabo, A. Dal Corso, S. de Gironcoli, S. Fabris, G. Fratesi, R. Gebauer, U. Gerstmann, C. Gougoussis, A. Kokalj, M. Lazzeri, L. Martin Samos, N. Marzari, F. Mauri, R. Mazzarello, S. Paolini, A. Pasquarello, L. Paulatto, C. Sbraccia, S. Scandolo, G. Sclauzero, A. P. Seitsonen, A. Smogunov, P. Umari and R. M. Wentzcovitch, *J. Phys. Condens. Matter.* 2009, **21**, 395502.
13. J. Zhang, P. Ming, B. Li and C. Zhang, *J. Mater. Chem. A* 2023, **11**, 20488-20496.
14. W. Yan, Q. Xing, J. Ren, H. Feng, J. Yu, H. Liu, W. Chen, K. Wang and Y. Chen, *Small* 2024, **20**, 2308473.
15. Z. Qiao, C. Wang, C. Li, Y. Zeng, S. Hwang, B. Li, S. Karakalos, J. Park, A. J. Kropf and E. C. Wegener, *Energ Environ. Sci.* 2021, **14**, 4948-4960.

16. X. Ao, W. Zhang, B. Zhao, Y. Ding, G. Nam, L. Soule, A. Abdelhafiz, C. Wang and M. Liu, *Energ Enviro. Sci.* 2020, **13**, 3032-3040.
17. L. Liang, H. Jin, H. Zhou, B. Liu, C. Hu, D. Chen, Z. Wang, Z. Hu, Y. Zhao and H. W. Li, *Nano Energy* 2021, **88**, 106221.
18. V. Bogdanovskaya, M. Tarasevich, L. Kuznetsova, G. Zhutaeva and O. Lozovaya, *Russ. J. Electrochem.* 2010, **46**, 925-933.
19. D. Wang, H. L. Xin, R. Hovden, H. Wang, Y. Yu, D. A. Muller, F. J. DiSalvo and H. D. Abruña, *Nat. Mater.* 2013, **12**, 81-87.
20. F. Xiao, Q. Wang, G. L. Xu, X. Qin, I. Hwang, C.-J. Sun, M. Liu, W. Hua, H. W. Wu and S. Zhu, *Nat. Catal.* 2022, **5**, 503-512.
21. S. Zaman, Y. Q. Su, C. L. Dong, R. Qi, L. Huang, Y. Qin, Y. C. Huang, F. M. Li, B. You and W. Guo, *Angew. Chem. Int.l Edit.* 2022, **61**, e202115835.
22. S. Zaman, X. Tian, Y. Q. Su, W. Cai, Y. Yan, R. Qi, A. I. Douka, S. Chen, B. You and H. Liu, *Sci. Bull.* 2021, **66**, 2207-2216.
23. Z. Wang, X. Yao, Y. Kang, L. Miao, D. Xia and L. Gan, *Adv. Funct. Mater.* 2019, **29**, 1902987.
24. L. Chong, J. Wen, J. Kubal, F. G. Sen, J. Zou, J. Greeley, M. Chan, H. Barkholtz, W. Ding and D. J. Liu, *Science* 2018, **362**, 1276-1281.
25. H. Niu, L. Huang, Y. Qin, R. Qi, B. Mei, D. Wu, F.-M. Li, B. You, Q. Li and Y. Yao, *J. Am. Chem. Soc.* 2024, **146**, 22650-22660.
26. Y. Wu, L. Chen, S. Geng, Y. Tian, R. Chen, K. Wang, Y. Wang and S. Song, *Adv. Funct. Mater.* 2024, **34**, 2307297.
27. Y. Nie, Y. Sun, B. Song, Q. Meyer, S. Liu, H. Guo, L. Tao, F. Lin, M. Luo and Q. Zhang, *Angew. Chem.* 2024, **136**, e202317987.
28. L. Gong, J. Zhu, F. Xia, Y. Zhang, W. Shi, L. Chen, J. Yu, J. Wu and S. Mu, *ACS Catal.* 2023, **13**, 4012-4020.
29. W. Zhu, Y. Pei, H. Liu, R. Yue, S. Ling, J. Zhang, X. Liu, Y. Yin and M. D. Guiver, *Adv. Sci.* 2023, **10**, 2206062.
30. P. Wang, K. Chen, J. Chen, G. Wang, W. Pan and Z. Wen, *Adv. Funct. Mater.* 2024, **34**, 2408267.
31. T. Hu, W. Chen, Y. Liu, L. Gong, Z. Jiang, D. Bhalothia, T. Maiyalagan and Z. J. Jiang, *Small* 2023, **19**, 2304076.
32. M. K. Jeon, Y. Zhang and P. J. McGinn, *Electrochim. Acta* 2010, **55**, 5318-5325.
33. I. Jang, S. Lee, D. g. Kim, V. K. Paidi, S. Lee, N. D. Kim, J. Y. Jung, K. S. Lee,

H. K. Lim and P. Kim, *Adv. Mater.* 2024, 2403273.

34. Z. Li, S. Ji, C. Xu, L. Leng, H. Liu, J. H. Horton, L. Du, J. Gao, C. He and X. Qi, *Adv. Mater.* 2023, **35**, 2209644.
35. Y. Jiao, X. Gu, P. Zhai, Y. Wei, W. Liu, Q. Chen, Z. Yang, J. Zuo, L. Wang and T. Xu, *Nano Lett.* 2022, **22**, 7386-7393.
36. Z. Liang, N. Kong, C. Yang, W. Zhang, H. Zheng, H. Lin and R. Cao, *Angew. Chem.* 2021, **133**, 12869-12874.
37. Z. Jiang, X. Liu, X. Z. Liu, S. Huang, Y. Liu, Z. C. Yao, Y. Zhang, Q. H. Zhang, L. Gu and L. R. Zheng, *Nat. Commun.* 2023, **14**, 1822.
38. T. Cui, Y. P. Wang, T. Ye, J. Wu, Z. Chen, J. Li, Y. Lei, D. Wang and Y. Li, *Angew. Chem. Int. Edit.* 2022, **61**, e202115219.
39. P. Cai, Y. Li, J. Chen, J. Jia, G. Wang and Z. Wen, *ChemElectroChem* 2018, **5**, 589-592.
40. H. Zhang, Z. Qu, H. Tang, X. Wang, R. Koehler, M. Yu, C. Gerhard, Y. Yin, M. Zhu and K. Zhang, *ACS Energy Lett.* 2021, **6**, 2491-2498.
41. C. Zhou, X. Chen, S. Liu, Y. Han, H. Meng, Q. Jiang, S. Zhao, F. Wei, J. Sun and T. Tan, *J. Am. Chem. Soc.* 2022, **144**, 2694-2704.
42. T. Tang, W. J. Jiang, X. Z. Liu, J. Deng, S. Niu, B. Wang, S. F. Jin, Q. Zhang, L. Gu and J. S. Hu, *J. Am. Chem. Soc.* 2020, **142**, 7116-7127.
43. L. An, Y. Li, M. Luo, J. Yin, Y. Q. Zhao, C. Xu, F. Cheng, Y. Yang, P. Xi and S. Guo, *Adv. Funct. Mater.* 2017, **27**, 1703779.
44. X. Yin, W. Sun, K. Chen, Z. Lu, J. Chen, P. Cai and Z. Wen, *Adv. Sci.* 2024, 2402343.
45. P. Cai, X. Peng, J. Huang, J. Jia, X. Hu and Z. Wen, *Sci. China Chem.* 2019, **62**, 385-392.
46. D. Gupta, A. Kafle, P. P. Mohanty, T. Das, S. Chakraborty, R. Ahuja and T. C. Nagaiah, *J. Mater. Chem. A* 2023, **11**, 12223-12235.
47. K. Wu, L. Zhang, Y. Yuan, L. Zhong, Z. Chen, X. Chi, H. Lu, Z. Chen, R. Zou and T. Li, *Adv. Mater.* 2020, **32**, 2002292.
48. D. Zhao, L. Zhang, S. Zuo, X. Lv, M. Zhao, P. Sun, X. Sun and T. L. Liu, *Small* 2023, **19**, 2206067.
49. J. Gao, D. Pan, K. Chen, Y. Liu, J. Chen and Z. Wen, *Adv. Energy Mater.* 2024, 2400368.